Mechanical Systems and Signal Processing 224 (2025) 112017

Contents lists available at ScienceDirect

Mechanical Systems and Signal Processing

journal homepage: www.elsevier.com/locate/ymssp

Non-contact vision-based response reconstruction and reinforcement learning guided evolutionary algorithm for substructural condition assessment

Guangcai Zhang [a,b,1], Jiale Hou [c,1], Chunfeng Wan [a,d,*], Jun Li [b], Liyu Xie [e], Songtao Xue [e,f]

[a] Key Laboratory of Concrete and Prestressed Concrete Structures of Ministry of Education, Southeast University, Nanjing, China
[b] Centre for Infrastructural Monitoring and Protection, School of Civil and Mechanical Engineering, Curtin University, Australia
[c] Department of Civil Engineering, Tsinghua University, Beijing, China
[d] Advanced Ocean Institute of Southeast University, Nantong, China
[e] Department of Disaster Mitigation for Structures, Tongji University, Shanghai 200092, China
[f] Department of Architecture, Tohoku Institute of Technology, Sendai, Japan

ARTICLE INFO

Keywords:
Substructural condition assessment
Vision-based measurement
Response reconstruction
Template matching algorithm
Sparse population initialization
Q-learning algorithm

ABSTRACT

Structural health monitoring of large-span bridges and high-rise buildings is crucial for ensuring safety and serviceability. However, accurately capturing motion in these structures using consumer-grade cameras is challenging due to their limited Field of Vision (FOV). To address this issue, in this study, a novel output-only substructural condition assessment framework based on the reinforcement learning-guided evolutionary algorithm and vision-based displacement response reconstruction technique is proposed. On the one hand, displacement responses of the target substructure are extracted from the vibration video using subpixel template matching algorithm with camera pose correction, which is suitable for integration with substructure strategy to detect elemental damage. A vision-based substructural displacement response reconstruction technique is developed based on transmissibility matrix and Tikhonov regularization. The measured and reconstructed displacements are utilized to established the objective function. On the other hand, to solve the optimization-based damage identification problem, a new reinforcement learning guided evolutionary algorithm, named sparse Q-learning guided evolutionary algorithm (SQEA), is proposed. In the proposed SQEA, sparse initial population is produced by reducing the dimension of unknown parameters to be identified. Six different search strategies, including DE/rand/1, DE/rand/2, DE/best/1, DE/best/2, Jaya mutation, perturbation with the Cauchy mutation, are used to construct a search strategy pool. A representative reinforced learning algorithm, Q-Learning algorithm is introduced to adaptively select the most suitable search strategy. Experimental tests on a steel frame structure and a three-span beam structure are performed to validate the accuracy, efficiency, and robustness of the proposed approach. Results demonstrate that the damage locations and extents can be accurately identified without the measurement of input forces, expanding the application of low-cost vision-based displacement

---

* Corresponding author at: Key Laboratory of Concrete and Prestressed Concrete Structures of Ministry of Education, Southeast University, Nanjing, China.

E-mail addresses: guangcaizhang@seu.edu.cn (G. Zhang), hjl23@mails.tsinghua.edu.cn (J. Hou), wan@seu.edu.cn (C. Wan), junli@curtin.edu.au (J. Li), liyuxie@tongji.edu.cn (L. Xie), xue@tongji.edu.cn (S. Xue).

[1] Guangcai Zhang & Jiale Hou contributed equally to this work, and should be considered as co-first authors.

https://doi.org/10.1016/j.ymssp.2024.112017
Received 12 May 2024; Received in revised form 2 October 2024; Accepted 3 October 2024

measurement in substructural condition assessment. Furthermore, the performance of the improved L-curve method over traditional L-curve and Bayesian inference regularization, the superiority of the proposed SQEA over other state-of-the-art intelligent algorithms are investigated.

1. Introduction

Over the past few decades, considerable infrastructures have been constructed, such as large-span bridges, concrete dams, spatial trusses, high-rise buildings, while they would inevitably accumulate damage during their long-term service period owing to fatigue, overload, aging, deterioration, earthquake, etc. Severe damage would result in adverse effects on the normal operation of the structures. Therefore, structural health monitoring (SHM) is crucial for ensuring the safety, reliability, and serviceability of these major civil structures. Traditional inspection methods, including visual inspections and specialized assessments, have limitations in terms of accuracy and efficiency. The increasing complexity and aging of infrastructures have driven the need for advanced SHM systems that go beyond traditional inspection methods. In recent years, numerous related researches have been implemented to perform continuous health monitoring, detect potential damage and assess the structural integrity at an early stage. The vibration-based damage identification methods, leveraging monitoring data from infrastructures to assess structural integrity, have attracted increasing attention [1–3]. Their fundamental idea is that damage-induced alternation in the structural physical properties like mass, damping, stiffness will cause detectable variation of dynamic characteristics, which can be used to inversely evaluate structural damage [4].

The vibration-based damage identification approaches can be roughly classified into frequency domain methods and time domain methods. For the former, eigenfrequencies [5], mode shapes [6], model strain energy [7], flexibility matrices [8], etc., are utilized to determine the health state of a structure, but these modal parameters are insensitive to minor damage and prone to be influenced by environmental variation and measurement noise, which limits their applications [9]. Time domain methods directly use the time histories of raw data, capturing more detailed information. Nevertheless, it was reported that substantial dynamic responses (displacements, strains, accelerations) are required, especially for the large-scale and complex structures because of many unknown parameters involved in the inverse analysis [10]. To address this limitation, substructure identification strategy [11] was proposed and received a lot of attention. Based on the straight idea of divide and conquer, the entire structure is divided into several substructures. Under a framework of substructure strategy, substructural parameters are detected and quantified individually and independently, which significantly improves the identification accuracy and computational efficiency since both the number of unknown parameters and degrees of freedom are largely reduced [12,13]. For example, Pan et al. [14] divided the structural elements into several groups and detected local damage by updating only part of the structural elements. The identified damage results of a cantilever beam in the laboratory are in good agreement with the actual values artificially introduced by cutting the cross-section. Huang et al. [15] utilized the element relative modal strain energy to identify substructural damage, and validated the effectiveness of the proposed method with experimental studies on a simply-supported beam structure.

Although conventional physical sensors such as linear variable displacement transducers (LVDT), strain gauges, accelerometers have been widely employed to measure structural responses, in practice, dense sensor networks need to be installed on the large-scale and complex civil structures owing to their point-wise measurement characteristic, which would be high-cost and time-consuming. Nowadays, with the development of video acquisition devices and computer vision techniques, some non-contact vison-based sensors have been increasingly used for structural health diagnosis owing to their merits of low cost, efficiency, multi-point sensing, and continuous monitoring [16–19]. A review of vision-based structural displacement measurement is given in Ref. [20]. In these vision-based methods, cameras [21], smartphones [22,23], etc., have been used to record the vibration videos. High accuracy for non-contact vision-based displacement measurement has been demonstrated by tracking the movement of pre-installed targets or other recognizable features on the structural surface [24]. Some scholars have extended the non-contact vision-based displacement measurement methods into the field of structural health monitoring in recent years because it is crucial to evaluate the safety of structure but challenging to direct measure [25]. For example, Feng et al. [26] utilized the output-only vision-based displacement data to simultaneously identify structural stiffness and external forces. Numerical and experimental studies on a simply supported beam proved the accuracy of the proposed method. Tan et al. [27] proposed a vision-based displacement measurement method, without the requirement of artificial target, for modal identification of a simply-supported bridge, i.e., natural frequencies and mode shapes. Cha et al. [28] combined the unscented Kalman filter and computer vision algorithm to predict the variation of structural parameters including stiffness and damping coefficients. Experimental tests on a cantilever beam showed that dynamic displacements could be accurately measured with the phase-based optical flow algorithm from video. The emerging non-contact vison-based measurement approaches are classified into four types in Ref. [29], i.e., template matching methods [30], optical flow methods [28], feature point tracking methods [10], video motion magnification methods [31,32]. Among them, template matching methods distinguish themself due to their merits of versatility and less human intervention [29].

By the literature review, there are few researches to combine the non-contact vision-based displacement measurement and substructure strategy. It is noted that the measurement range of vision-based measurement methods may be constrained by the Field of Vision (FOV) of cameras, especially for a large-scale and complex structure. In addition, the accuracy of multi-point displacement measurements would be deteriorated over a wider field of view. Although advanced photographic equipment with a wide-range lens could be used to address this limitation, this solution substantially increases the cost of implementing vision-based displacement measurement [27]. Instead, if the vibration videos of the interested substructure are concentrated on, higher accuracy in displacement measurement with only one consumer-grade camera or smartphone will be achieved. Thus, it is suitable for combining non-contact vision-based displacement measurement with substructure strategies to detect local elemental damage. Nevertheless, the coexist of unknown forces and local damage poses a huge challenge for the application of vision-based displacement measurements. To eliminate the requirement of force measurement in substructural damage identification, a vision-based displacement response reconstruction technique in time domain based on transmissibility matrix and Tikhonov regularization is developed, expanding the application of low-cost vision-based displacement measurement for structural health monitoring.

Traditional filter-based methods, iterative least-squares method, response sensitivity-based method, generally need a good initial estimate and gradient information. In contrast, intelligent algorithms [33], especially for evolutionary algorithms, have attracted extensive attention, such as improved particle swarm optimization [34], accelerated differential evolution algorithm (ADE) [35], modified Artificial Bee Colony algorithm [36], modified Jaya algorithm [37], whale optimization algorithm [38], to solve the optimization-based inverse damage identification problem owing to their powerful global search capacity and good robustness [39]. For instance, Zhou et al. [40] presented an improved butterfly optimization algorithm for identifying structural parameters with the aid of sampling technique and search space reduction method. Wu et al. [41] developed a multi-objective salp swarm algorithm to identify parameters of concrete dams, and used Gaussian process as surrogate model. The computational time can be significantly reduced owing to eliminating extensive finite element simulations. However, most intelligent optimization algorithms rely on fixed operations, and the search operation is relatively single and monotonous, making it difficult to achieve the balance between global exploration and local exploitation. Besides, a single swarm intelligence algorithm often struggles to address diverse optimization problems effectively. Selecting the optimal evolutionary operators manually maybe labor-intensive and time-consuming.

Inspired by the idea that different search strategies have different optimization performances, to deal with this issue, multiple search strategies with reinforcement learning algorithm have been explored [42,43], while sparse population and random perturbation are not considered in these papers. In this study, six representative search strategies including DE/rand/1, DE/rand/2, DE/best/1, DE/best/2, Jaya mutation, perturbation with the Cauchy mutation, are used to construct a search strategy pool. It is noted that these search strategies have their own characteristics and play different roles. During the searching process, individuals will adaptively select the most appropriate search strategy under the guidance of Q-learning algorithm at each iteration. Additionally, damage often occur in a small number of elements, while most of them are intact. In this end, sparse population initialization method is introduced to reduce

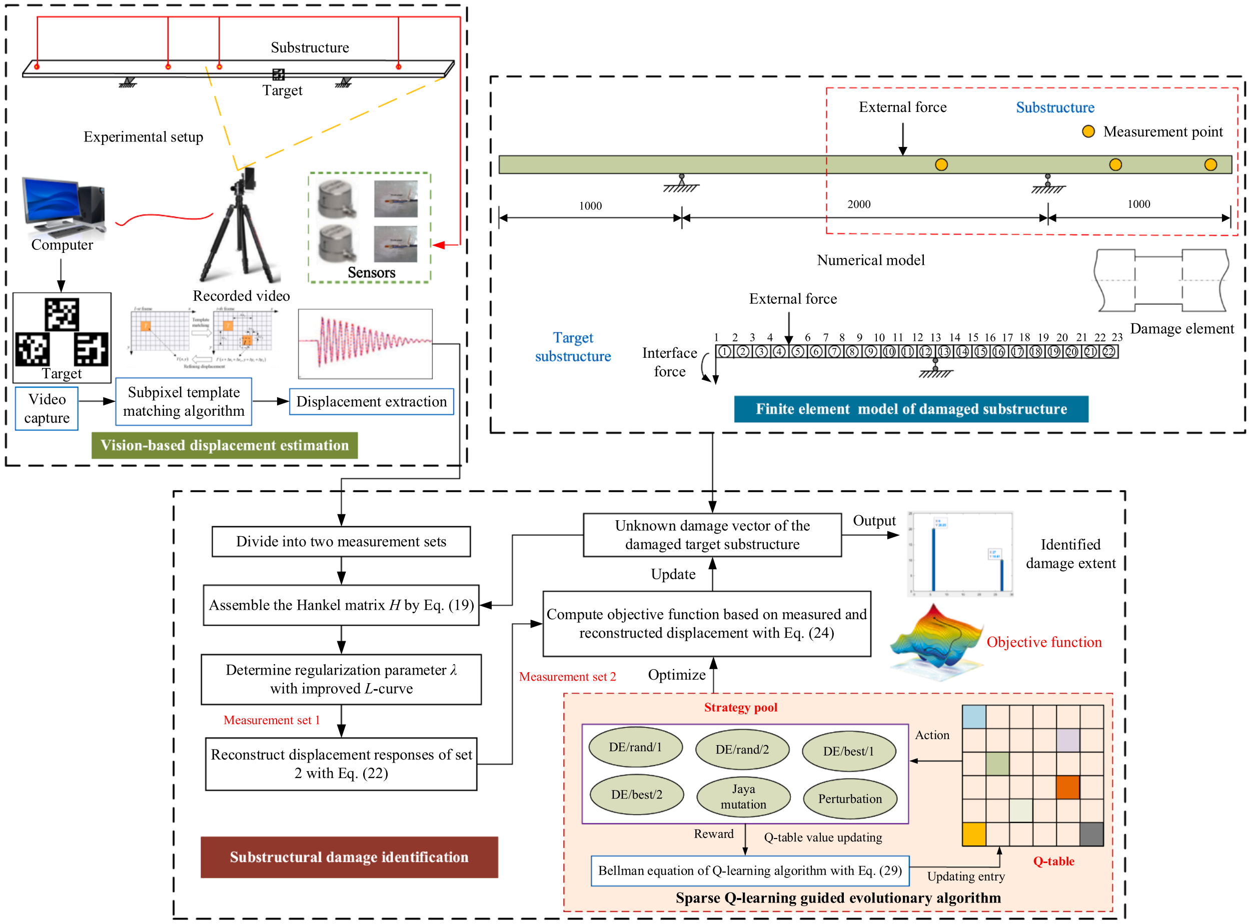

Fig. 1. The workflow of the proposed substructural damage identification method.

the dimension of unknown parameters.

The major contributions of the present research are as follows:

1) A new output-only substructural damage identification method is proposed based on the noncontact vision-based displacement response reconstruction. The potentials of low-cost vision-based displacement data are explored for modal identification and substructural damage identification. The problem of limited FOV of cameras in long structure's monitoring is addressed.
2) A novel reinforcement learning guided evolutionary algorithm, sparse Q-learning guided evolutionary algorithm (SQEA), is developed enabling an adaptive selection of the best search operation from strategy pool in each iteration, offering a corporation framework for more evolutionary algorithms and reinforcement learning.
3) Experimental tests on a steel frame structure and a three-span beam structure in the laboratory validate the effectiveness of the proposed approach in substructural damage identification.

This rest of the paper is organized as follows. Section 2 presents the subpixel template matching algorithm for computer vision-based displacement measurement, and then introduces substructural displacement response reconstruction technique in time domain. In Section 3, the objective function is formulated based on the measured and reconstructed displacement data. Sparse Q-learning guided evolutionary algorithm is proposed, which includes sparse population initialization, strategy pool of evolutionary algorithm and Q-learning algorithm. The specific implementation procedures of the proposed approach are elaborated in Section 4. Section 5 shows two experimental cases to verify the proposed output-only substructural damage method. In Section 6, concluding remarks are summarized and the feasible research direction is given.

2. Vision-based displacement response reconstruction

The flowchart of the proposed substructural condition assessment method based on non-contact vision-based response reconstruction and reinforcement learning guided evolutionary algorithm is provided in Fig. 1. Vision-based displacement measurement and response reconstruction, and substructural damage identification are introduced in Section 2 and Section 3, respectively.

2.1. Displacement extraction with template matching algorithm

The vision-based multipoint displacement measurement method with template matching algorithm is shown in Fig. 2. Firstly, the pixel level coordinate of the selected target can be easily obtained using cross correlation-based method [44], and then subpixel level image registration [45] is used to get the subpixel level coordinate. Lastly, the scaling factor is used to transform the pixel displacement into real-world displacement. Herein, the technical details are elaborated as follows.

Supposed that the image is $S(x,y)$ with dimension $E \times N$ and template image is $U(x,y)$ with dimension $A \times B$. Firstly, to ensure the results of cross-correlation are not affected by the brightness and contrast of the image, zero mean normalization on the template image and target image is performed, respectively

$$\overline{S}(x,y) = S(x,y) - \frac{1}{EN}\sum_{i=1}^{E}\sum_{j=1}^{N} T(i,j), \quad \overline{U}(x,y) = U(x,y) - \frac{1}{AB}\sum_{i=1}^{A}\sum_{j=1}^{B} I(i,j) \tag{1}$$

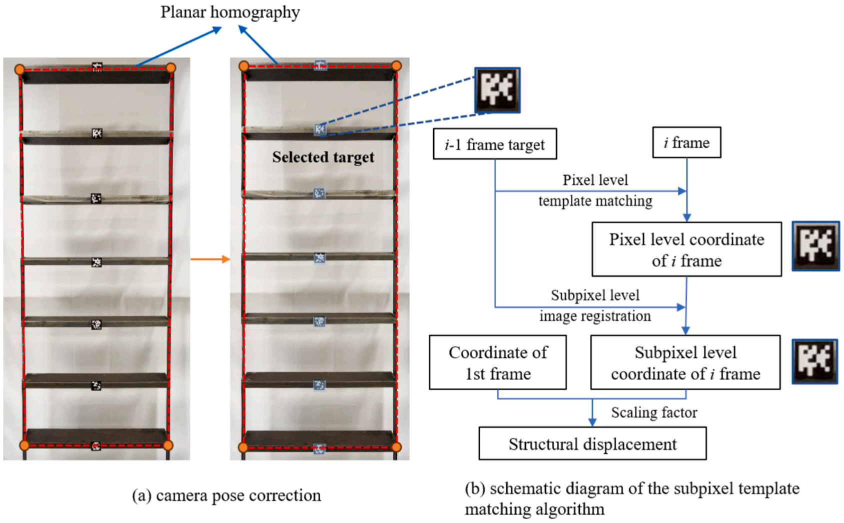

(a) camera pose correction (b) schematic diagram of the subpixel template matching algorithm

Fig. 2. The non-contact vision-based displacement measurement.

Then, the cross correlation between $\overline{S}(x,y)$ and $\overline{U}(x,y)$ can be defined as

$$R(x_0,y_0) = \sum_{x,y} \overline{S}(x,y)\overline{U}^*(x-x_0,y-y_0) \tag{2}$$

where (x_0,y_0) is the coordinate offset and $\overline{U}^*(x-x_0,y-y_0)$ means the zero-padding of original $\overline{U}(x,y)$ to make it consistent with the image size of $\overline{S}(x,y)$. To accelerate this calculation process, the convolution theorem is used as follows

$$R(x_0,y_0) = \sum_{u,v} \widehat{S}(\mu,v)\widehat{U}^*(\mu,v)\exp[i2\pi(\frac{\mu x_0}{E}+\frac{\mu y_0}{N})] \tag{3}$$

$$\widehat{S}(\mu,v) = \sum_{x,y} \frac{\overline{S}(x,y)}{\sqrt{EN}}\exp[-i2\pi(\frac{\mu x}{E}+\frac{\mu y}{N})] \tag{4}$$

where $\widehat{S}(\mu,v)$, $\widehat{U}(\mu,v)$ are the discrete Fourier transform (DFT) of $\overline{S}(x,y)$ and $\overline{U}(x,y)$, and '*' means complex conjugation. Therefore, the pixel coordinate of the target can be obtained by locating the maximum of the $R(x_0,y_0)$.

Subsequently, the subpixel level target identification is conducted using a subpixel image registration algorithm [45]. The cross correlation in a 1.5×1.5 pixel neighborhood around the initial estimation is up-sampled using matrix-multiplication DFT operation by an up-sampling factor k. This operation is implemented by the product of three matrices with dimension $(1.5k,E)$, (E,N), $(N,1.5k)$. Then, the subpixel resolution displacement within $1/k$ can be obtained by locating the maximum of the up-sampled cross correlation matrix. The up-sampling factor k in this paper is set to 100, which means 0.01 subpixel level displacement can be calculated. Finally, it is noted that the scaling factor serves as a crucial intermediary, transforming the conversion of pixel displacement values into their corresponding real-world counterparts, and its unit is *mm/pixel*.

Ideally, the camera's optical axis is perpendicular to the surface of the structure, so the scaling factor can be obtained by directly dividing the physical scale by the corresponding pixel scale. However, due to various factors such as on-site conditions and instrument equipment, it is usually difficult for the camera's optical axis to remain completely perpendicular to the structural surface, which significantly increases the errors in displacement measurement [46]. To solve this problem, projection transformation method is used to correct the camera pose to a position that the optical axis perpendicular to the structural plane. Firstly, select four rectangular points of the target structural plane from the first frame of the video and then project the points onto the manually defined regular rectangular coordinates. Then, the Homography matrix is computed with following equation

$$\begin{bmatrix} x_2 \\ y_2 \\ 1 \end{bmatrix} = \begin{bmatrix} \delta_{00} & \delta_{01} & \delta_{02} \\ \delta_{10} & \delta_{11} & \delta_{12} \\ \delta_{20} & \delta_{21} & \delta_{22} \end{bmatrix} \begin{bmatrix} x_1 \\ y_1 \\ 1 \end{bmatrix} \tag{5}$$

where (x_1,y_1) is the coordinate of the point in the first frame; (x_2,y_2) is the coordinate of the point in the corrected image; $[\delta_{00}, \delta_{01},\ldots, \delta_{22}]$ is undetermined coefficient vector.

All points in the first frame and subsequent frames of the video can be projected to the corrected images. In this way, the scaling factor calculated using the corrected image will be more accurate than the calculated using the original image.

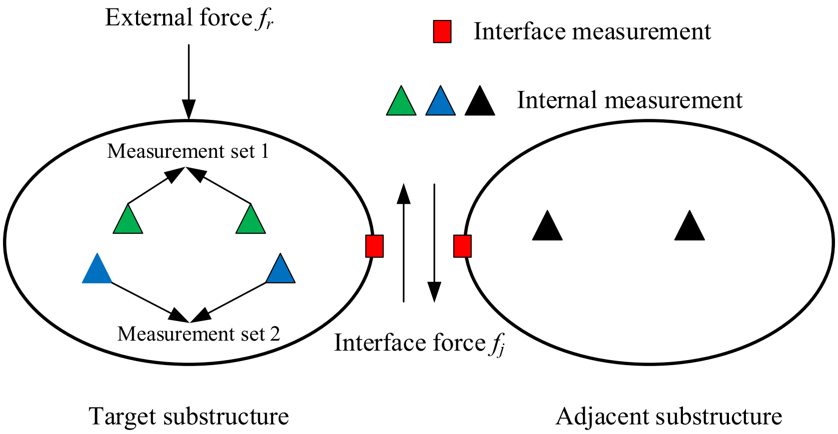

Fig. 3. The schematic diagram of forces and responses of the substructure.

2.2. Substructural displacement response reconstruction

The equation of dynamic motion for a multiple degrees of freedom linear structural system can be described as

$$M\ddot{u}(t) + C\dot{u}(t) + Ku(t) = Lf(t) \tag{6}$$

where M, C, K are the mass, damping, stiffness matrices of a structural system; $\ddot{u}(t)$, $\dot{u}(t)$, $u(t)$ are the acceleration, velocity, displacement responses when the structure is subjected to external load $f(t)$; L represents the mapping matrix associated with the force location. Structural mass can be directly estimated with geometric dimensions and material properties. Rayleigh damping model $C = \beta_1 M + \beta_2 K$ is employed, where damping coefficients β_1 and β_1 could be determined by the damping ratios of first two modes.

Substructural identification strategy [11] rooted in the fundamental principle of divide and conquer, aims to accelerate the process of damage identification. By dividing the entire structure into several substructures, the iterative task of calculating dynamic responses is alleviated. This substructural identification strategy proves advantageous in augmenting convergence speed and computational efficiency, owing to a significant reduction in both unknown parameters and degrees of freedom.

The dynamic equation of the target substructure, as shown in Fig. 3, can be expressed as

$$\begin{bmatrix} M_{rj} & M_{rr} \end{bmatrix} \begin{bmatrix} \ddot{u}_j(t) \\ \ddot{u}_r(t) \end{bmatrix} + \begin{bmatrix} C_{rj} & C_{rr} \end{bmatrix} \begin{bmatrix} \dot{u}_j(t) \\ \dot{u}_r(t) \end{bmatrix} + \begin{bmatrix} K_{rj} & K_{rr} \end{bmatrix} \begin{bmatrix} u_j(t) \\ u_r(t) \end{bmatrix} = L_r f_r(t) \tag{7}$$

where r and j stand for the internal and interface degrees of freedom.

If the interface forces are regarded as unknown input, Eq. (7) can be rewritten as

$$M_{rr}\ddot{u}_r(t) + C_{rr}\dot{u}_r(t) + K_{rr}u_r(t) = L_r f_r(t) - \left(M_{rj}\ddot{u}_j(t) + C_{rj}\dot{u}_j(t) + K_{rj}u_j(t) \right) \tag{8}$$

On the right side of the equation above, $L_r f_r(t)$ represents the external load acting on the target substructure and $L_j f_j(t) = M_{rj}\ddot{u}_j(t) + C_{rj}\dot{u}_j(t) + K_{rj}u_j(t)$ denotes the interface force of adjacent substructure. Considering the external loads and interface forces acting on the substructure as equivalent input forces of the substructure, Eq. (8) can be rewritten as follows

$$M_{rr}\ddot{u}_r(t) + C_{rr}\dot{u}_r(t) + K_{rr}u_r(t) = Lf(t) \tag{9}$$

$$Lf(t) = L_r f_r(t) - L_j f_j(t)$$

According to the superposition theory for a linear structure subjected to multiple forces, displacement response at the p-th Dof can be calculated by

$$u_p(t_n) = u_{p,1}(t_n) + u_{p,2}(t_n) + , \dots, + u_{p,nf}(t_n) = \sum_{i=1}^{nf} u_{p,i}(t_n) \tag{10}$$

where $u_{p,i}(t_n)$ denotes the displacement response from the p-th Dof subjected to the i-th force at time t_n; nf represents the total number of unknown equivalent input forces of the substructure, including external forces and interface forces.

Based on the Duhamel integral, the displacement response $u_{p,i}(t_n)$ at the p-th Dof under the i-th force $f_i(t)$ can be calculated by

$$u_{p,i}(t_n) = \int_0^{t_n} h_{p,i}(t_n - \tau) f_i(\tau) d\tau \tag{11}$$

where $h_{p,i}(t_n)$ stands for the displacement impulse response function, and it can be obtained by Newmark method

$$\begin{cases} M_{rr}\ddot{h}_r(t) + C_{rr}\dot{h}_r(t) + K_{rr}h_r(t) = 0 \\ h_r(0) = 0, \dot{h}_r(0) = M_{rr}^{-1} L \end{cases} \tag{12}$$

When Eq. (11) is substituted into Eq. (10), substructural displacement response $u_p(t_n)$ can be obtained by

$$u_p(t_n) = \sum_{i=1}^{nf} \int_0^{t_n} h_{p,i}(t_n - \tau) f_i(\tau) d\tau \tag{13}$$

The discretized form of Eq. (13) is expressed as follows

$$u_p(t_n) = \sum_{i=1}^{nf} h_{p,i}(t_n) f_i(t_n) \tag{14}$$

The displacement response from t_0 to t_n at the p-th Dof location could be rewritten as

$$\begin{bmatrix} u_p(t_0) \\ u_p(t_1) \\ u_p(t_2) \\ \vdots \\ u_p(t_n) \end{bmatrix} = \sum_{i=1}^{nf} \begin{bmatrix} h_{p,i}(t_0) & 0 & 0 & 0 & 0 \\ h_{p,i}(t_1) & h_{p,i}(t_0) & 0 & 0 & 0 \\ h_{p,i}(t_2) & h_{p,i}(t_1) & h_{p,i}(t_0) & 0 & 0 \\ \vdots & \vdots & \vdots & \ddots & \vdots \\ h_{p,i}(t_n) & h_{p,i}(t_{n-1}) & h_{p,i}(t_{n-2}) & \cdots & h_{p,i}(t_0) \end{bmatrix} \begin{bmatrix} f_i(t_0) \\ f_i(t_1) \\ f_i(t_2) \\ \vdots \\ f_i(t_n) \end{bmatrix} \tag{15}$$

Then, Eq. (15) is easily simplified as

$$Y_u = \sum_{i=1}^{nf} H_{u,i} F_i \tag{16}$$

where substructural displacement output is $Y_u = \left[u_p(t_0), u_p(t_1), ..., u_p(t_n)\right]^T$ and external input is $F_i = \left[f_i(t_0), f_i(t_1), ..., f_i(t_n)\right]^T$; displacement impulse response function matrix under the i-th force is

$$H_{u,i} = \begin{bmatrix} h_{p,i}(t_0) & 0 & 0 & 0 & 0 \\ h_{p,i}(t_1) & h_{p,i}(t_0) & 0 & 0 & 0 \\ h_{p,i}(t_2) & h_{p,i}(t_1) & h_{p,i}(t_0) & 0 & 0 \\ \vdots & \vdots & \vdots & \ddots & \vdots \\ h_{p,i}(t_n) & h_{p,i}(t_{n-1}) & h_{p,i}(t_{n-2}) & \cdots & h_{p,i}(t_0) \end{bmatrix} \tag{17}$$

In fact, computer vision can realize displacement measurement of multiple points with several tracking targets. Accordingly, the equation between multiple displacement responses and input forces can be further expressed as

$$Y = HF \tag{18}$$

where $Y = [Y_{n1}, Y_{n2}, ..., Y_{nu}]^T$, nu stands for the number of sensor locations; $F = \left[f_1, f_2, ..., f_{nf}\right]^T$; Hankel matrix H is

$$H = \begin{bmatrix} H_{n1,1} & H_{n1,2} & H_{n1,3} & \cdots & H_{n1,nf} \\ H_{n2,1} & H_{n2,2} & H_{n2,3} & \cdots & H_{n2,nf} \\ H_{n3,1} & H_{n3,2} & H_{n3,3} & \cdots & H_{n3,nf} \\ \vdots & \vdots & \vdots & \ddots & \vdots \\ H_{nu,1} & H_{nu,2} & H_{nu,3} & \cdots & H_{nu,nf} \end{bmatrix} \tag{19}$$

In Eq. (18), the dimensions of Y, H, F, are $(nu \times t_n) \times 1$, $(nu \times t_n) \times (nf \times t_n)$, $(nf \times t_n) \times 1$.

According to response reconstruction technique in time domain [47], in this study, substructural multipoint displacements from noncontact vision sensor are divided into two measurement sets, i.e., measurement set 1 Y_{mea}^{set1} and measurement set 2 Y_{mea}^{set2}. Substructural displacements Y_{mea}^{set1} and Y_{mea}^{set2} can be represented as

$$\begin{cases} Y_{mea}^{set1} = H_1 F \\ Y_{mea}^{set2} = H_2 F \end{cases} \tag{20}$$

There exists no explicit equation for the classification of vision-based displacement measurements into two different sets, while it is imperative that the number of measurements within the first set surpasses or equals the unknown equivalent loads, which is essential for guaranteeing the success of pseudo-inverse $(H_1)^+$. Under this condition, equivalent loads can be obtained by $F = (H_1)^+ Y_{mea}^{set1}$. Subsequently, the displacement measurements of set 2 are reconstructed with following equation

$$Y_{rec}^{set2} = H_2 (H_1)^+ Y_{mea}^{set1} = T_{12} Y_{mea}^{set1} \tag{21}$$

where T_{12} is transmissibility matrix, $T_{12} = H_2 (H_1)^+$.

Obviously, transmissibility matrix is the function of unknown structural parameters. In other word, displacement measurements of set 2 Y_{rec}^{set2} can be acquired when the first set of measurements and structural parameters are known. Nevertheless, it is noted that unbounded or poor solutions may be obtained in solving the inverse problem with ordinary least square method, especially taking the measurement noise into account. Herein, to stabilize the solution process, a damped least square method, i.e., Tikhonov regularization, is introduced as

$$Y_{rec}^{set2} = H_2 \left(H_1^T H_1 + \lambda I\right)^{-1} H_1^T Y_{mea}^{set1} \tag{22}$$

where λ represents the regularization parameter.

The key issue for Tikhonov regularization technique is how to properly select the optimal regularization parameter. Different from traditional *L*-curve method, the improved *L*-curve technique incorporating *B*-spline interpolation function proposed by authors [37] is employed to choose the parameter in consideration of its high stability and low computational cost. The implementation procedures of the improved *L*-curve technique are roughly divided into three primary steps. Initially, the conventional *L*-curve method is used to construct an initial plot. Subsequently, a localized region proximate to the *L*-corner is identified for *B*-spline interpolation. Finally, the determination of the optimal regularization parameter is facilitated through an analysis of the curvature exhibited by the nodal points within this delineated region. More detailed introduction about this technique can be found in Zhang et al. [37].

3. Substructural damage identification

3.1. Damage model and objective function

The structural/substructural damage is generally modeled as a reduction in local property, such as elemental stiffness loss, and the alternation of mass is not considered [36,37]. The damaged structure remains linear elastic, and its global stiffness matrix is expressed as

$$K^d = \sum_{e=1}^{ne}(1-\alpha_e)K_e^{\mathrm{ele}}, 0\leqslant\alpha_e\leqslant1 \tag{23}$$

where K^d and K_e^{ele} stand for the stiffness matrix of damaged structure and the *i*-th elemental stiffness matrix in healthy state, respectively; *ne* denotes the number of elements. A series of elemental damage vectors $\alpha_e = \frac{E_e - E_e^d}{E_e}$, $e = 1, \ldots, ne$ are introduced to describe the local damage model. $\alpha_e = 1$ indicates the *e*-th element is totally damaged and $\alpha_e = 0$ means this element is intact.

The inverse problem of damage identification can be transformed into an optimization problem. The objective function is defined as the difference between the measured displacement responses Y_{mea}^{set2} from the damaged substructure and reconstructed measurement set 2 $Y_{rec}^{set2}(\alpha)$ using the proposed vision-based displacement response reconstruction technique as follows

$$\min\ f_{obj}(\alpha) = \left\| Y_{mea}^{set2} - Y_{rec}^{set2}(\alpha) \right\|_2 \tag{24}$$

where $\|\cdot\|_2$ means the l_2 norm; objective function $f_{obj}(\alpha)$ is zero when the reconstructed displacement responses are equal to the measured responses, and the unknown substructural damage are accurately identified.

3.2. Sparse Q-learning guided evolutionary algorithm

To solve the optimization-based inverse problem, a novel reinforcement learning guided optimization framework is proposed in this study. In the optimization framework, we develop a sparse Q-learning guided evolutionary algorithm, which effectively combines sparse population initialization, strategy pool of evolutionary algorithm and Q-learning algorithm. In the following subsections, the details of these contents are individually introduced.

3.2.1. Sparse population initialization

For the traditionary evolutionary algorithms, such as genetic algorithm, differential evolution algorithm, initial population is randomly generated within the predefined lower and upper search limits. Each individual in the colony stands for a candidate solution. Random population initialization would result in most components of candidate solutions ranging from 0 and 1, which obviously conflicts with the actual situation of the damage identification problem. As a matter of fact, damage tend to occur on a few elements, while most of them are intact, i.e., elemental damage vectors α_e equal or very close to zero. To achieve the sparse damage vector α_e, considering the known information about the damaged structure, a sparse population initialization method is introduced into basic evolutionary algorithm, and its pseudo-code is shown in Fig. 4.

Initially, generate a candidate solution where each component is zero. Then, determine the number of assumed damaged elements D_e as follows

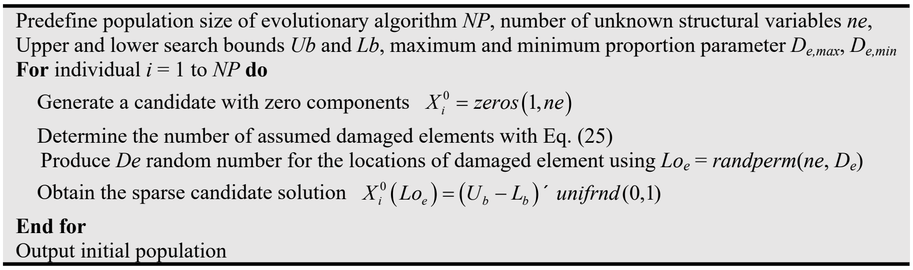

```
Predefine population size of evolutionary algorithm $NP$, number of unknown structural variables $ne$,
Upper and lower search bounds $Ub$ and $Lb$, maximum and minimum proportion parameter $D_{e,max}$, $D_{e,min}$
For individual $i = 1$ to $NP$ do
    Generate a candidate with zero components  $X_i^0 = zeros(1, ne)$
    Determine the number of assumed damaged elements with Eq. (25)
    Produce $De$ random number for the locations of damaged element using $Lo_e = randperm(ne, D_e)$
    Obtain the sparse candidate solution  $X_i^0(Lo_e) = (U_b - L_b)'\ unifrnd(0,1)$
End for
Output initial population
```

Fig. 4. The pseudo-code of sparse population initialization.

$$D_e = ceil\left[\left(D_{e,\min} + \left(D_{e,\max} - D_{e,\min}\right) \times rand\right) \times ne\right] \tag{25}$$

where *ceil* represents the function that rounds to the next higher integer; *rand* and *ne* stand for the random numbers uniformly distributed in the interval [0, 1] and number of elements, respectively; $D_{e,\max}$ and $D_{e,\min}$ are two parameters corresponding to the maximum and minimum proportion of damaged elements among all elements.

The value of $D_{e,\max} \times ne$ should be less than the total number of structural elements, and $D_{e,min} \times ne$ must not be less than the number of actual damaged elements. Subsequently, produce D_e random number to determine the locations of damaged elements. Finally, the population of evolutionary algorithm is sparsely generated.

For individuals generated by the sparse population initialization method, only small components are assigned random values within the range [0, 1]. This strategy enhances the probability of locating candidates within or near favorable regions of the search space, where optimal solutions are likely to reside. Consequently, for the new evolutionary algorithm, convergence speed is accelerated and computational resource is notably reduced.

3.2.2. Strategy pool

DE algorithm has been wildly used to solve various optimization problems, while it is difficult for basic DE algorithm to balance the global exploration and local exploitation using only single local search strategy. To this end, a strategy pool with six different search strategies is developed to enrich the search patterns by calculating diverse solutions in a single run. In the proposed strategy pool, DE/rand/1, DE/rand/2, DE/best/1, DE/best/2, Jaya mutation, perturbation with the Cauchy mutation play different roles, mutually complement, and collaboratively evolve

$$Strategy\,pool = \begin{cases} DE\begin{cases} Exploration \quad group\begin{cases} DE/rand/1 \\ DE/rand/2 \end{cases} \\ Exploitation \quad group\begin{cases} DE/best/1 \\ DE/best/2 \end{cases} \end{cases} \\ non - DE\begin{cases} Jayamutation \\ Perturbation \quad with \quad Cauchy \quad mutation \end{cases} \end{cases} \tag{26}$$

where exploration group consists of DE/rand/1 and DE/rand/2 mutation strategies; exploitation group contains DE/best/1 and DE/best/2 mutation strategies; non-DE part includes Jaya mutation and perturbation with the Cauchy mutation.

The Eq. (26) can be mathematically expressed as

$$Strategy\,pool = \begin{cases} V_{i,G} = X_{r_1,G} + F\left(X_{r_2,G} - X_{r_3,G}\right) \\ V_{i,G} = X_{r_1,G} + F\left(X_{r_2,G} - X_{r_3,G}\right) + F\left(X_{r_4,G} - X_{r_5,G}\right) \\ V_{i,G} = X_{best,G} + F\left(X_{r_1,G} - X_{r_2,G}\right) \\ V_{i,G} = X_{best,G} + F\left(X_{r_1,G} - X_{r_2,G}\right) + F\left(X_{r_3,G} - X_{r_4,G}\right) \\ V_{i,G} = X_{i,G} + rand_1 \times \left(X_{best,G} - \left|X_{i,G}\right|\right) - rand_2 \times \left(X_{worst,G} - \left|X_{i,G}\right|\right) \\ X'_{best,j,G} = X_{best,j,G} \times (1 + Cauchy(z_0, \varepsilon)) \end{cases} \tag{27}$$

where $V_{i,G}$ means the i-th mutation vector at the G-th iteration; $X_{r_1,G}$, $X_{r_1,G}$, $X_{r_1,G}$, $X_{r_1,G}$ denote randomly selected individuals, $i \neq r_1 \neq r_2 \neq r_3 \neq r_4$; F represents the positive mutation coefficient; $rand_1$ and $rand_2$ are random numbers within [0, 1]; $X_{best,G}$ and $X_{worst,G}$ are the best solution and worst one, respectively; $X'_{best,j,G}$ is the j-th dimension of the updated best candidate solution; $Cauchy(z_0, \varepsilon)$ stands for a random number obtained from the standard Cauchy distribution.

In Eq. (26), individuals in the DE/rand/1 and DE/rand/2 mutation strategies from exploration group are randomly selected, endowing them with strong global search capability, thereby reducing the likelihood of falling into local optima and ensuring population diversity. Nonetheless, these strategies exhibit slower convergence rates. Conversely, for the exploitation group, the DE/best/1 and DE/best/2 mutation strategies utilize the best individual of the current population, resulting in powerful local search capability and rapid convergence, while they are susceptible to fall into local optima and fail to guarantee population diversity. Jaya mutation is the key operation of Jaya algorithm, and its core idea is that updated individuals in the population would move towards the best solution and away from the worst solution, which enables Jaya algorithm to acquire the optimal solution with higher possibilities.

By DE/best/1, DE/best/2, Jaya mutation in Eq. (27), the updated individuals are closely associated with the current-best-solution. In fact, the best solution $X_{best,G}$ plays a pivotal role during the iteration process by exerting a guiding and attracting influence on the other individuals to relocate towards its position. However, when dealing with complex optimization problems characterized by multimodal and multipeak, the current-best-solution may be trapped within a local optimum, resulting in premature convergence. To prompt the current-best solution to jump out from the local optima, herein, perturbation with the Cauchy mutation is introduced as

$$f_{\varepsilon}(z) = \frac{1}{\pi}\frac{\varepsilon}{\varepsilon^2 + (z - z_0)^2}, \quad \varepsilon > 0, \quad -\infty < z < +\infty \tag{28}$$

where $f_{\varepsilon}(z)$ denotes the standard Cauchy distribution function; ε and z_0 stand for a proportion parameter and peak position, respectively, $\varepsilon = 1, \quad z_0 = 0$.

In contrast to the Gaussian distribution, the Cauchy distribution exhibits a reduced peak at the origin while displaying an elongated distribution at both ends. Hence, Cauchy mutation can induce a greater perturbation in proximity to the current-best-individual than Gaussian mutation, facilitating an easier escape from local optima. The perturbation with the Cauchy mutation serves to mitigate the risk of premature convergence to local optima.

3.2.3. Framework of the proposed algorithm

Q-learning algorithm [43] is popular choice enabling individuals to adaptively select the most appropriate local search operation from the strategy pool. As a model-free reinforcement learning technique, Q-learning algorithm has five main components, i.e., a learning agent, an environment, actions, states, and rewards, and its fundamental concept revolves around a learning agent's responsiveness to changes of states, driven by immediate rewards or penalties. With each iteration, the agent would evaluate all potential actions and perform the most optimal action, aiming to maximize future rewards or minimize penalties by prioritizing those with the highest Q-values.

Assuming a learning agent has a set of states $S = \{s_1, s_2, ..., s_n\}$ and corresponding actions $A = \{a_1, a_2, ..., a_n\}$ to be conducted. The update equation of Q-value $Q^{new}(s_t, a_t)$ for the action a_t in state s_t can be calculated using Bellman equation as [48]

$$Q^{new}(s_t, a_t) = Q(s_t, a_t) + \varphi[w_{t+1} + \gamma \cdot \max Q(s_{t+1}, a_t) - Q(s_t, a_t)] \tag{29}$$

where φ is the learning rate; w_{t+1} represents the reward or penalty for potential action a_t; γ denotes the discount factor within the range of [0,1] involving imposing penalties on future rewards, suggested $\gamma = 0.8$; $\max Q(s_{t+1}, a_t)$ stands for the maximum value of Q-table. Learning rate φ determines the degree of the new value accepted, and its equation is $\varphi(Iter) = 1 - 0.9 \times \frac{Iter}{Max\_Iter}$, in which *Iter* and *Max_Iter* are current and maximum iteration number, respectively.

A Q-learning guided evolutionary optimization framework is proposed by properly combining the Q-learning algorithm and multiple search strategies. In the proposed framework, the sparsely generated individuals are regarded as the learning agents; the environment stands for the search domain of the unknown parameters; the states are viewed as the updating operations in strategy pool, i.e., DE/rand/1, DE/rand/2, DE/best/1, DE/best/2, Jaya mutation, perturbation with the Cauchy mutation; the action is considered as the alteration from one state to another. More specifically, six states correspond to six actions. The size of Q-table is 6 by 6. In Fig. 5, a diagram illustrates the transition from the current state to the next within the Q-table framework. The individual selects an action based on the highest Q-value for the current state, for example, DE/rand/1. If DE/best/1 has the highest Q-value, the algorithm updates the next state to DE/best/1, corresponding to the same index as the selected action. By repeating this process iteratively, the algorithm enables dynamic selection and execution between states and actions, optimizing performance adaptively.

The best action for the current state will be adaptively selected and implemented based on the maximum Q-table value

$$best\ action = Max[Q(current\ state, \quad all\ actions)] \tag{30}$$

Positive rewards and negative rewards are assigned to these search strategies based on their performance in each iteration. Positive rewards are granted to strategies with improved performance, while penalties, in the form of negative rewards, are given to underperformed ones

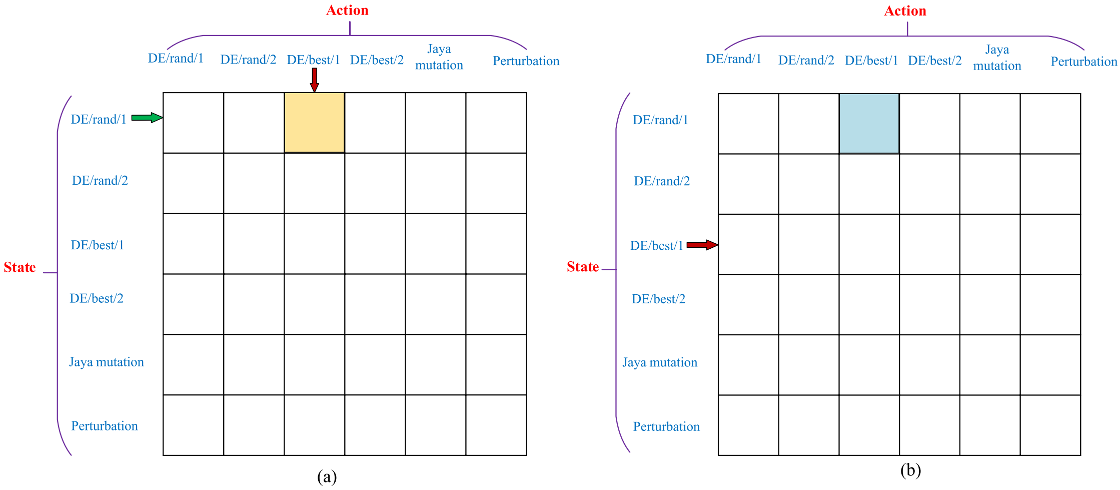

Fig. 5. Updating diagram of the Q-table.

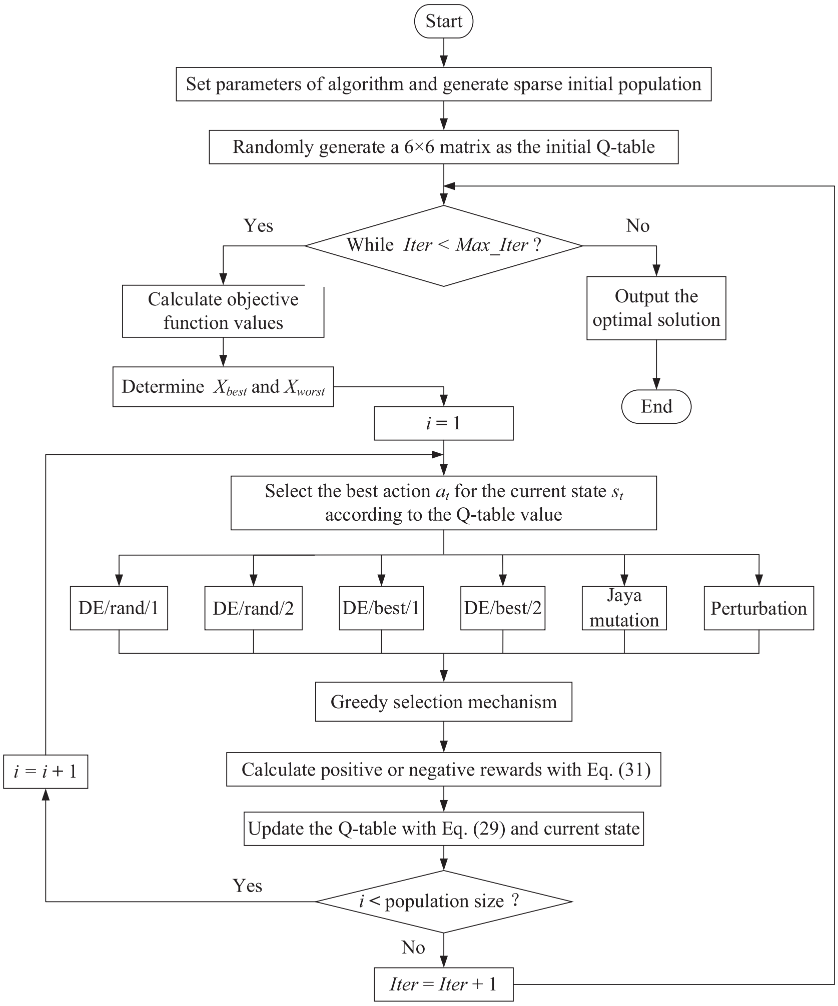

Fig. 6. The structure of the proposed SQEA.

$$w_t = \begin{cases} 1 & \textit{if } f_{obj} \text{ is improved} \\ -1 & \textit{otherwise} \end{cases} \tag{31}$$

The sparse Q-learning guided evolutionary algorithm (SQEA) is proposed by integrating sparse population initialization, strategy pool and Q-learning algorithm. The structure of the proposed SQEA is shown in Fig. 6.

Clearly, SQEA has a simple structure and it is easy to operate. Individuals are generated within the promising regions of the search domain using sparse population initialization. Strategy pool provides multiple search operations to enrich the candidate solutions. The Q-learning algorithm is used to select the most appropriate search strategy using the information accumulated in the Q-table at each iteration.

4. Implementation procedures

For detecting the presence, location, and severity of damage in the substructure, a noncontact vision-based displacement measurement, response reconstruction, and sparse Q-learning guided optimization framework are developed. The specific implementation procedures are illustrated as follows:

Step 1: Preinstall the standard target on the surface of substructure and place a smartphone or a camera at a certain distance from the target substructure to record the vibration video subjected to external force.

Step 2: Obtain the multipoint displacement histories using template matching algorithm with camera pose correction and divide them into measurement set 1 Y_{mea}^{set1} and measurement set 2 Y_{mea}^{set2}.

Step 3: Construct the finite element model of the target substructure.

Step 4: Predefine the parameters of the proposed SQEA and generate the sparse initial population.

Step 5: Calculate the transmissibility matrix T_{12}, and reconstruct the displacement measurement set 2 Y_{rec}^{set2} using the first set of displacement measurements and current stiffness with Eq. (22).

Step 6: Transform the damage identification problem into an optimization process wherein the objective is to minimize the discrepancies between the measured and reconstructed displacement responses of measurement set 2 given in Eq. (24).

Step 7: Optimize the objective function with the proposed SQEA by iteratively updating the unknown elemental damage vectors of the target substructure. In this process, the most proper operation is adaptively selected from the strategy pool under the guide of Q-learning algorithm.

Step 8: Repeat Step 3 to Step 7 until the convergence criteria is met. Finally, output the identified substructural damage results.

5. Experimental investigations

To verify the proposed substructural condition assessment method, experimental investigations on an eight-floor steel frame structure and a three-span beam structure are conducted. All analyses are implemented in the environment of MATLAB R2020a using a personal computer equipped with Intel(R) Core i5- 13600KF CPU @ 3.50 GHz and 16.0 GB of RAM.

5.1. Steel frame structure

5.1.1. Experimental setup

The experimental tests on a steel frame structure are carried out in the laboratory, as shown in Fig. 7(a). Based on the geometric dimensions illustrated in Fig. 7(b), the total height and length of the frame model are 2.0 m and 0.6 m. The rectangular cross-sections of two columns and eight beams are 50 mm × 5 mm and 100 mm × 25 mm, respectively. The steel material employed in this experiment is characterized by a mass density of 7850 $\mathrm{kg/m^3}$ and an initial elastic modulus of $2.06 \times 10^{11}\mathrm{N/m^2}$. The columns and beam elements are welded together and treated as rigid joints, and the bottoms of the two columns are fixed to a thick steel plate. Two different finite element models are considered, i.e., 8-Dofs FE model and 48-Dofs FE model. The 8-Dofs model is a shear-type lumped mass model and the relatively complex 48-Dofs model has 16 nodes and 24 planar frame elements. Eight PCB-393B04 accelerometers are mounted on the steel frame structures to record acceleration responses at each floor. Impulse load is applied to the top floor of steel frame model using a hammer with a rubber tip. The sampling frequency and sampling duration are set as 1200 Hz and 60 s, respectively.

To achieve substructural damage identification using the noncontact vision-based displacement measurement, a series of tracking targets are attached on the surface of each beam element with a size of 30 mm × 30 mm. The steel frame model is excited by impact

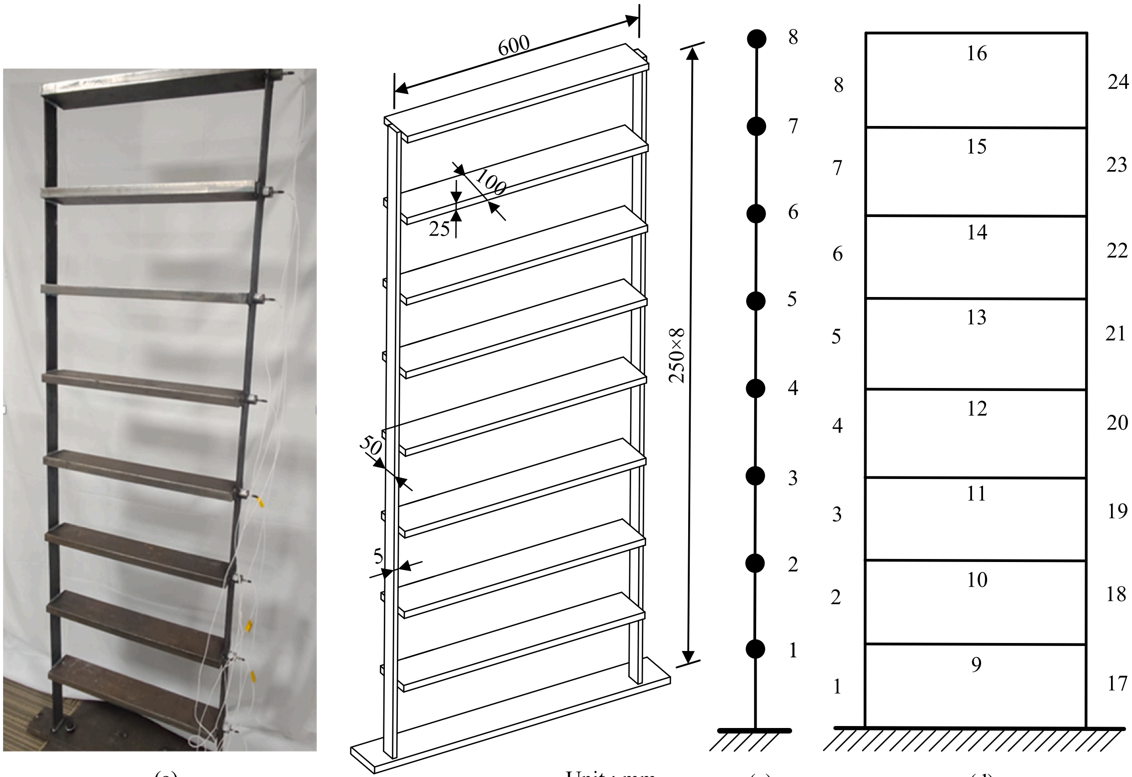

(a) (b) (c) (d)

Fig. 7. Eight-floor frame structure: (a) experimental setup; (b) geometric dimensions; (c) 8-Dofs FE model; (d) 48-Dofs FE model.

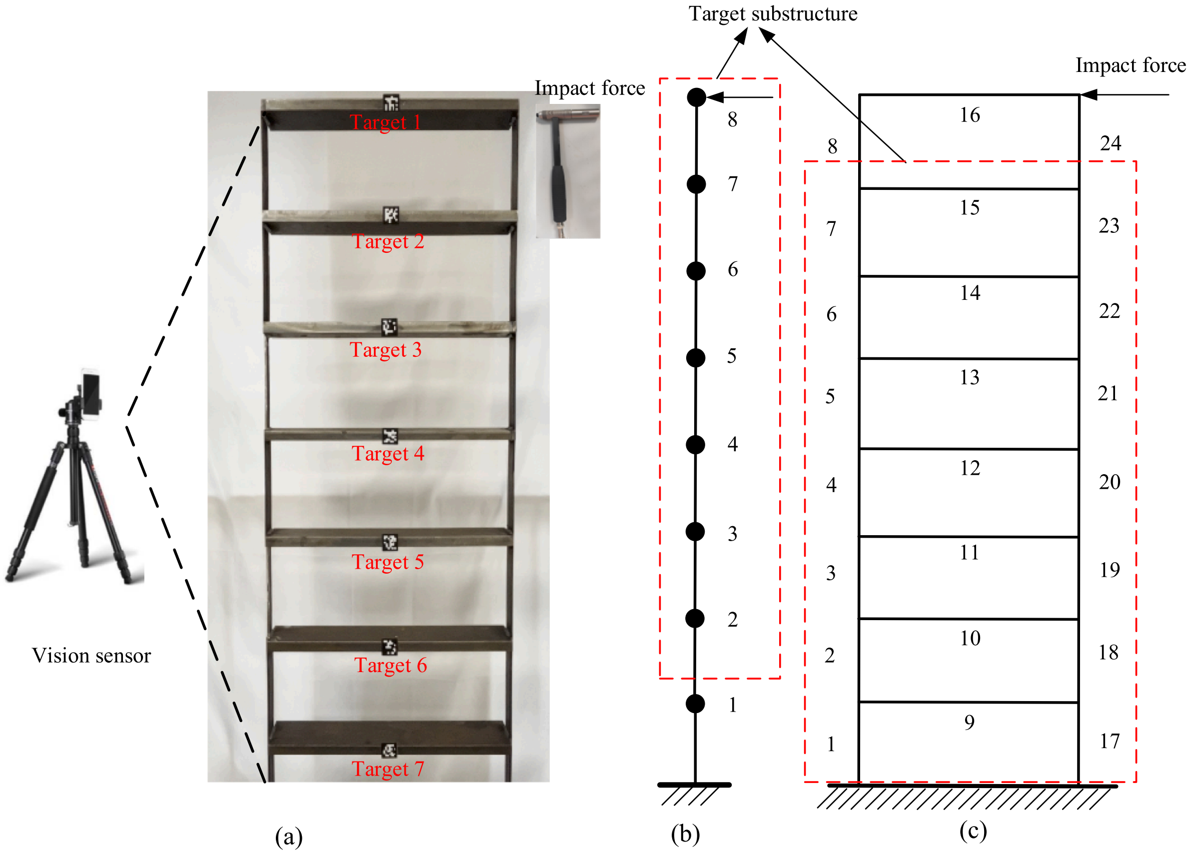

Fig. 8. The vision-based measurement for substructural damage identification: (a) test setup; (b) target substructure of 8-Dofs model; (c) target substructure of 48-Dofs model.

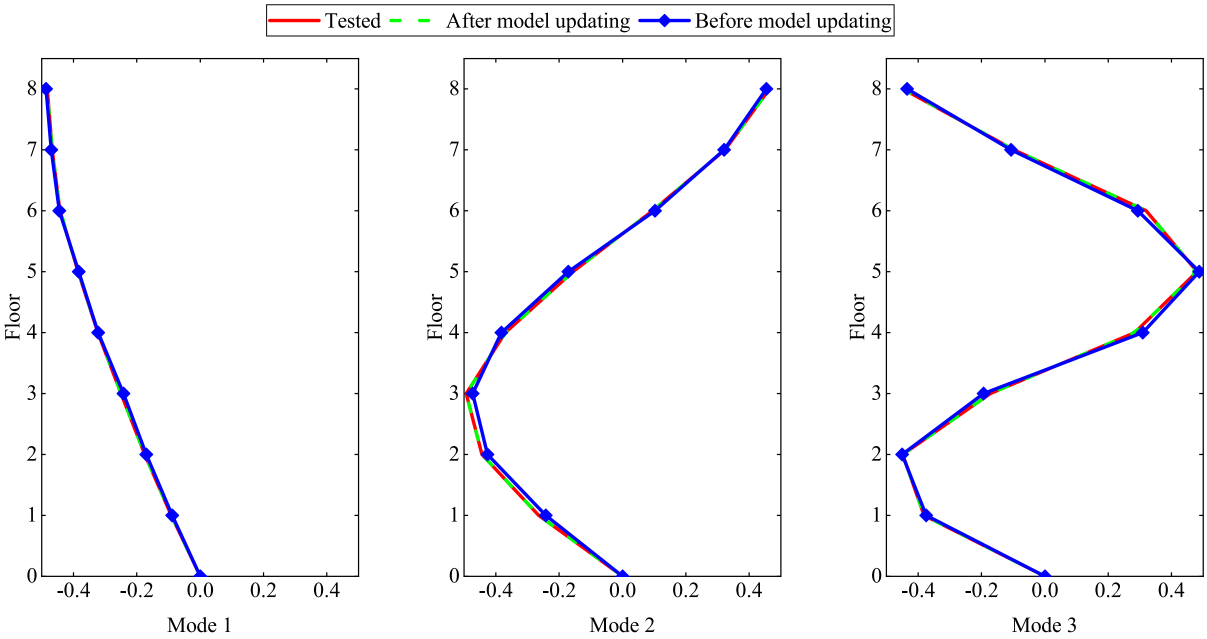

Fig. 9. The first three mode shapes of steel frame structure.

hammer at the top floor. As depicted in Fig. 8(a), a smartphone is used as a vision sensor to record the vibration histories during the test with the sampling rate of 60 frames per second (fps) and a resolution of 3840 × 2160 pixel. Displacement time histories are extracted using subpixel template matching algorithm with camera pose correction by processing the video images frame by frame. Fig. 8(b) and 8(c) present the target substructures of 8-Dofs model and 48-Dofs model defined in this example, respectively.

5.1.2. 8-Dofs FE model

5.1.2.1. Initial model updating. Initial model updating of steel frame structure in healthy status is conducted to minimize the discrepancy between the experimental model and numerical model. Acceleration responses from eight sensors are utilized to update the 8-Dofs lumped mass model. The tested and analytical mode shapes and natural frequencies before and after updating are provided in Fig. 9 and Table 1, respectively. It can be observed that there are relatively large errors of natural frequencies with the maximum error of 3.811 % before updating, while the updated model has a good agreement with the tested structure, with a maximum error of 0.057 % after model updating. In this end, updated finite element model can be taken as the baseline model for the subsequent displacement response reconstruction and substructural damage identification. Besides, the first third natural frequencies of vision-based displacements by Fast Fourier Transform are 4.502 Hz, 13.941 Hz and 22.485 Hz, which closely match the 4.510 Hz, 13.865 Hz, 22.753 Hz obtained by accelerations, proving the feasibility of non-contact vision measurement to some extent.

5.1.2.2. Displacement response reconstruction under undamaged state. After implementing initial model updating for the target substructure in healthy state, the non-contact vision-based displacement response reconstruction method proposed in Section 2 is validated. As presented in Fig. 8(b), the 2nd to 8th floors of the steel frame model is selected as the target substructure. One external force at the 8th floor and one interface force acting on the first floor are treated as unknown excitations. Displacements from 2nd to 8th floors are obtained by the subpixel template matching algorithm, and they are divided into two different sets. Measurement set 1 has the displacement responses from 2nd, 4th, 6th, 8th floors, which is larger than the total number of unknown forces applied to the substructure, and the measurement set 2 includes the displacement responses from 3rd, 5th, 7th floors. The measured displacements of the first 30 s data in measurement set 1 are depicted in Fig. 10(a). It can be found that the magnitude of dynamic displacements gradually decays after hammer impact excitation.

The displacement responses at the floors 3, 5, and 7 in measurement set 2 are reconstructed based on the dynamic responses in measurement set 1 and the updated finite element model. The displacement time histories used for reconstruction are selected from 0.5 s to 10.5 s, as shown in Fig. 10(b). Herein, relative percentage error (*RPE*) and Pearson correlation coefficient (*PCC*) are used to reflect the difference between the measured displacement responses Y_{mea} and the reconstructed values Y_{rec} in the measurement set 2 as follows

$$RPE = \frac{\|Y_{rec} - Y_{mea}\|_2}{\|Y_{mea}\|_2} \times 100\% \tag{32}$$

$$PCC(Y_{mea}, Y_{rec}) = \frac{Cov(Y_{mea}, Y_{rec})}{\sigma_{Y_{mea}}\sigma_{Y_{rec}}} \tag{33}$$

where $Cov(Y_{mea}, Y_{rec})$ represents the covariance of variables Y_{mea} and Y_{rec}; $\sigma_{Y_{mea}}$ and $\sigma_{Y_{rec}}$ stand for the standard deviation of Y_{mea} and Y_{rec}.

Fig. 11 shows the comparison of the reconstructed displacement responses with the measured ones. It is evident that the reconstructed responses at the 5th and 7th floors in measurement set 2 can match well with the displacement data extracted from the recorded video. More specifically, *RPE* are 5.16 % and 4.08 %, and *PCC* are 0.9996 and 0.9999 corresponding to the 5th and 7th floors, respectively. Thus, a good accuracy of non-contact vision-based displacement response reconstruction is achieved.

5.1.2.3. Damage identification results. As shown in Fig. 12, damage is artificially introduced by reducing the cross-section of one column. It is noted that 20 % cross-section reduction in one column is equivalent to 10 % stiffness reduction in this floor. Likewise, 40 % cross-section reduction in one column results in 20 % equivalent stiffness reduction. Four different damage cases including single damage and multiple damage are considered. Damage case 1: 10 % stiffness reduction in the 4th floor, i.e., $\alpha_4 = 0.1$; Damage case 2: 20 % stiffness reduction in the 4th floor, i.e., $\alpha_4 = 0.2$; Damage case 3: 20 % stiffness reduction in the 4th floor and 10 % stiffness reduction in the 6th floor, i.e., $\alpha_4 = 0.2$ and $\alpha_6 = 0.1$; Damage case 4: 20 % stiffness reduction in the 4th floor and 20 % stiffness reduction in the 6th floor, i.e., $\alpha_4 = 0.2$ and $\alpha_6 = 0.2$.

Table 1
The measured and updated natural frequencies of steel frame structure.

Mode	Before updating		After updating		Tested values from accelerations (Hz)
	Analytical (Hz)	Relative error (%)	Analytical (Hz)	Relative error (%)	
1	4.382	2.820	4.508	0.025	4.510
2	14.394	3.811	13.867	0.014	13.865
3	22.960	0.906	22.766	0.057	22.753

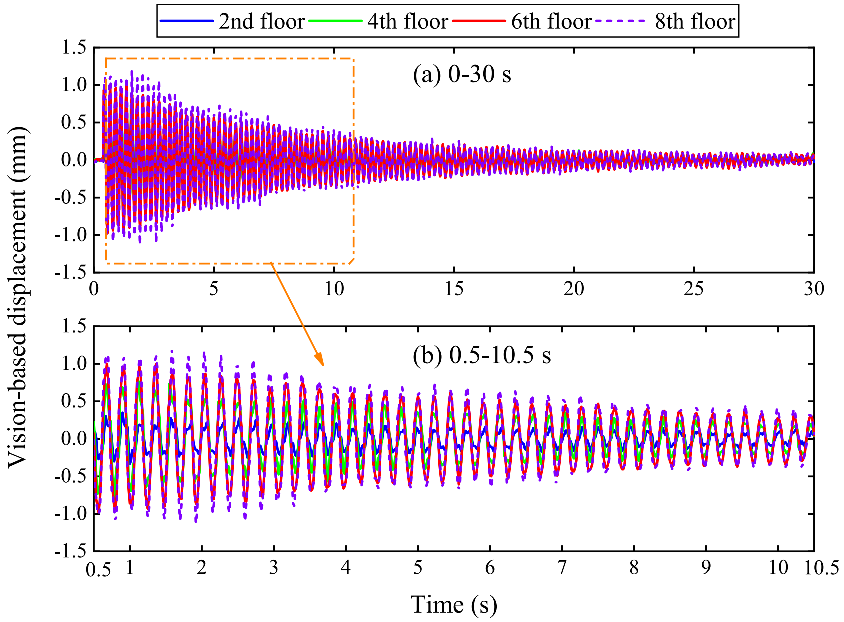

Fig. 10. The measured displacements in set 1 under the undamaged state: (a) the first 30 s; (b) 0.5–10.5 s.

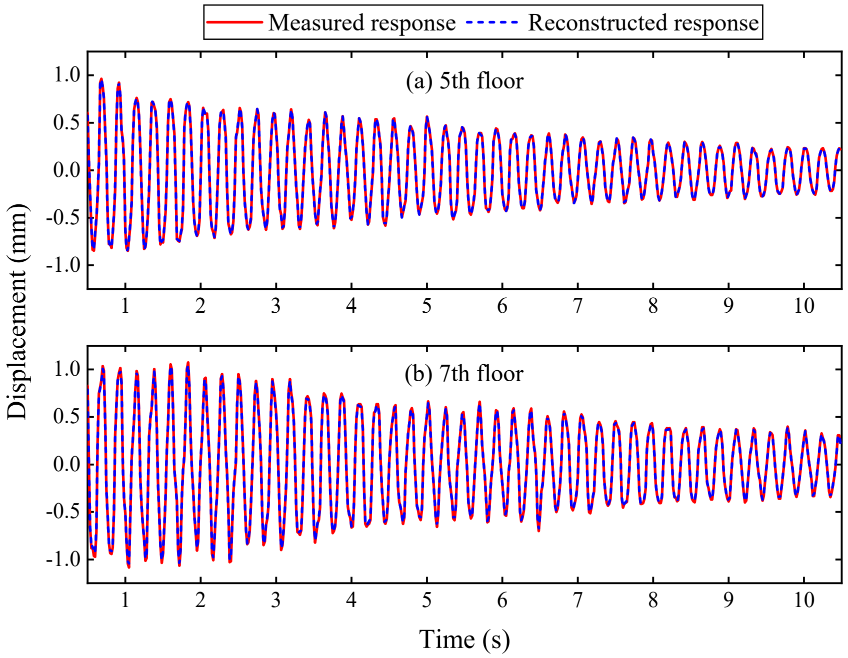

Fig. 11. The reconstructed and measured displacement responses: (a) 5th floor; (b) 7th floor.

To determine the optimal regularization parameter, the improved L-curve technique incorporating B-spline interpolation function is utilized in this study. To demonstrate its superiority, damage identification results based on the traditional L-curve method of Tikhonov regularization technique [49] and Bayesian inference regularization method [50] are employed and compared. The objective function is optimized by the proposed SQEA. The parameters of SQEA are: population size $NP = 60$, the maximum number of iterations $Max\_Iter = 100$, discount factor $\gamma = 0.8$. The identified damage results for the target substructure of 8-Dofs model are shown in Fig. 13 and Table 2. Clearly, both damage locations and severities are successfully detected for four damage cases. As listed in Table 2, the maximum errors acquired by traditional L-curve method are 5.41 %, 6.51 %, 4.88 %, 4.73 % corresponding to damage case 1, case 2, case 3, case 4, which are obviously larger than 2.25 %, 1.69 %, 2.10 %, 3.52 % for the improved L-curve technique, also larger

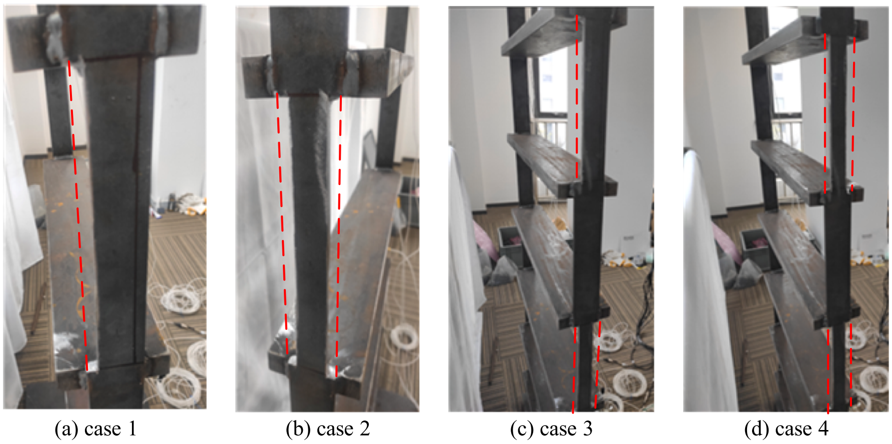
(a) case 1 (b) case 2 (c) case 3 (d) case 4

Fig. 12. Four different damage cases of eight-floor steel frame structure.

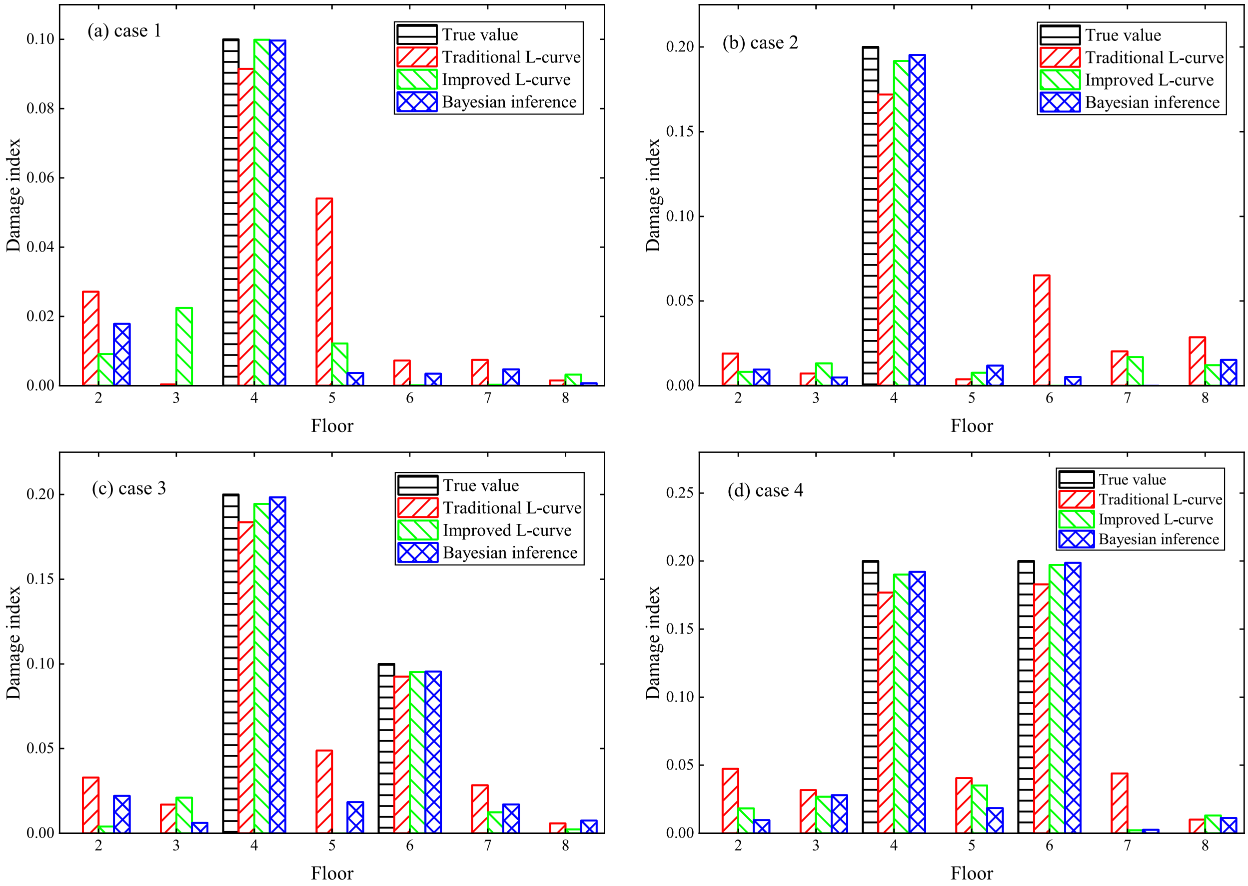

Fig. 13. Identified damage results of the target substructure: (a) case 1; (b) case 2; (3) case 3; (d) case 4.

than 1.79 %, 1.52 %, 2.21 %, 2.80 % for Bayesian inference regularization method. Considering the adverse effect of measurement noise and modeling errors, these results reasonably prove the effectiveness of the proposed improved L-curve technique incorporating B-spline interpolation function in displacement response reconstruction and damage detection.

5.1.3. 48-Dofs FE model

As presented in Fig. 8(c), one to seven floors of the 48-Dofs FE model are selected as the target substructure. The hammer impact force is applied to the top floor. There are six unknown interface forces acting on the substructure and 21 unknown stiffness damage

Table 2
Identified errors with traditional, improved L-curve and Bayesian inference regularization methods (%).

Type of responses	Damage cases	Traditional L-curve		Improved L-curve		Bayesian inference regularization	
		Mean error	Max error	Mean error	Max error	Mean error	Max error
Displacement	Case 1	1.52	5.41	0.68	2.25	0.44	1.79
	Case 2	2.46	6.51	0.95	1.69	0.73	1.52
	Case 3	2.24	4.88	0.72	2.10	1.10	2.21
	Case 4	3.05	4.73	1.55	3.52	1.13	2.80
Acceleration	Case 1	1.46	5.87	0.60	2.34	0.42	1.83
	Case 2	2.18	6.94	0.88	2.03	0.69	1.62
	Case 3	2.09	4.77	0.69	2.25	0.63	1.99
	Case 4	2.86	4.61	1.52	3.33	1.20	2.66

indexes to be identified. Vison-based displacements from the 1st to 7th floors acquired by the subpixel template matching algorithm are divided into two different sets. Measurement set 1 contains the displacement responses from floors 1, 2, 3, 4, 6, 7, which is not less than the total number of interface forces on the substructure, and the measurement set 2 includes the displacement response from floor 5. The displacement response at the 5th floor is reconstructed based on the dynamic responses in measurement set 1 and the updated finite element model. The discrepancy between the reconstructed and measured displacement responses are defined as objective function, iteratively optimized with the proposed SQEA until the convergence criterion is satisfied.

Four different damage cases including single damage and multiple damage are considered, i.e., 20 % stiffness reduction in element 4 for case 1, 40 % stiffness reduction in element 4 for case 2, 40 % and 20 % stiffness reductions in element 4 and element 6 for case 3, 40 % and 40 % stiffness reductions in element 4 and element 6 for case 4. Fig. 14 and Table 3 provide the identified results for these damage cases. It can be observed that all damaged elements in case 1, case 2, case 3, case 4 are almost accurately localized and quantified. More specifically, in case 1 and case 2, the identified damage extents at element 4 are 18.18 % and 35.39 %, matching well with the actual values of 20 % and 40 %. In case 3 and case 4, the identified damage extents in the 4th element are 34.86 % and 35.62 %, in the 6th element are 16.48 % and 37.96 %, respectively. There are apparent identification errors, as listed in Table 3, the maximum and mean errors in damage case 4 are 9.20 % and 2.11 %, which is reasonable and acceptable since more unknown parameters are identified than 8-Dofs model with same number of displacement measurements under the adverse effect of measurement

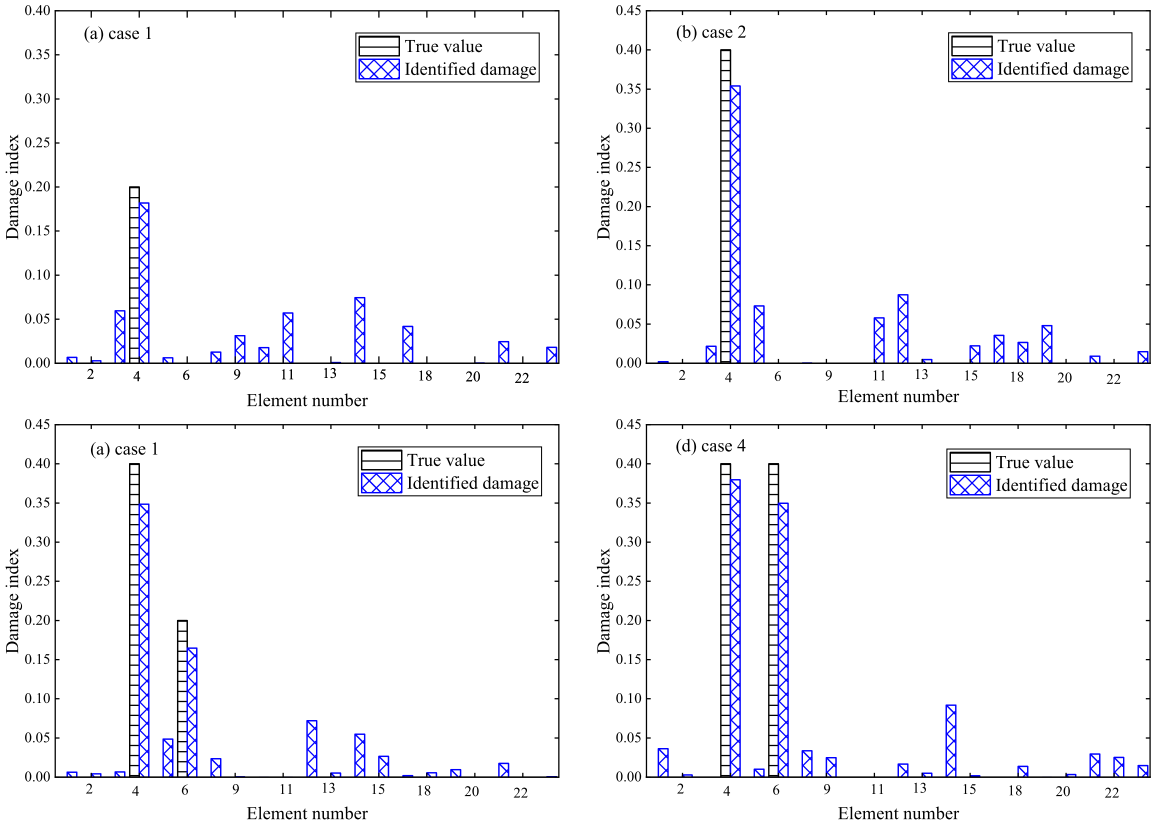

Fig. 14. The identified damage results for the target substructure of 48-Dofs model: (a) case 1; (b) case 2; (3) case 3; (d) case 4.

Table 3
Identified damage indexes and relative errors for the four damage cases.

Type of responses	Damage cases	Damage index for element 4			Damage index for element 6			Identified error (%)	
		True value	Identified	RE*	True value	Identified	RE*	Max	Mean
Displacement	Case 1	0.2	0.1818	9.08 %				7.44	1.77
	Case 2	0.4	0.3539	11.52 %				8.73	2.14
	Case 3	0.4	0.3486	12.84 %	0.2	0.1648	17.60 %	7.21	2.01
	Case 4	0.4	0.3562	10.95 %	0.4	0.3796	5.11 %	9.20	2.11
Acceleration	Case 1	0.2	0.1827	8.65 %				8.02	1.63
	Case 2	0.4	0.3571	10.73 %				7.29	2.08
	Case 3	0.4	0.3523	11.93 %	0.2	0.1682	15.90 %	7.11	1.97
	Case 4	0.4	0.3617	9.58 %	0.4	0.4265	6.62 %	8.54	2.04

Note: RE* means the relative error.

noise and modeling errors.

By Table 2 and Table 3, it can be found that similar calculation results are obtained by using acceleration response and non-contact vision-based displacement response, which shows that the proposed substructure damage identification method based on noncontact vision-based displacement response reconstruction and SQEA has both the identification accuracy of contact acceleration response and advantages of non-contact measurement.

5.2. Three-span beam structure

5.2.1. Experimental setup

To further validate the performance of the proposed method for substructural damage identification through vision-based displacement measurement, a laboratory experiment is conducted on a three-span beam structure, as shown in Fig. 15(a). By the configuration, the three-span continuous beam has a total length of 4000 mm and a rectangular cross-section of 50 mm × 16 mm, and it is discretized into 40 Euler-Bernoulli beam elements with 41 nodes and 80 Dofs, as presented in Fig. 15(b). As for the constraint condition, there are a hinge support at the node 11 and a roller support at the node 31. The details of the roller support and hinge support are provided. In addition, to obtain the displacement responses, artificial targets, as shown in Fig. 15(c), are attached on the substructures. The elastic modulus and mass density of steel material are 206 GPa and 7850 kg/m^3, respectively. An impact load

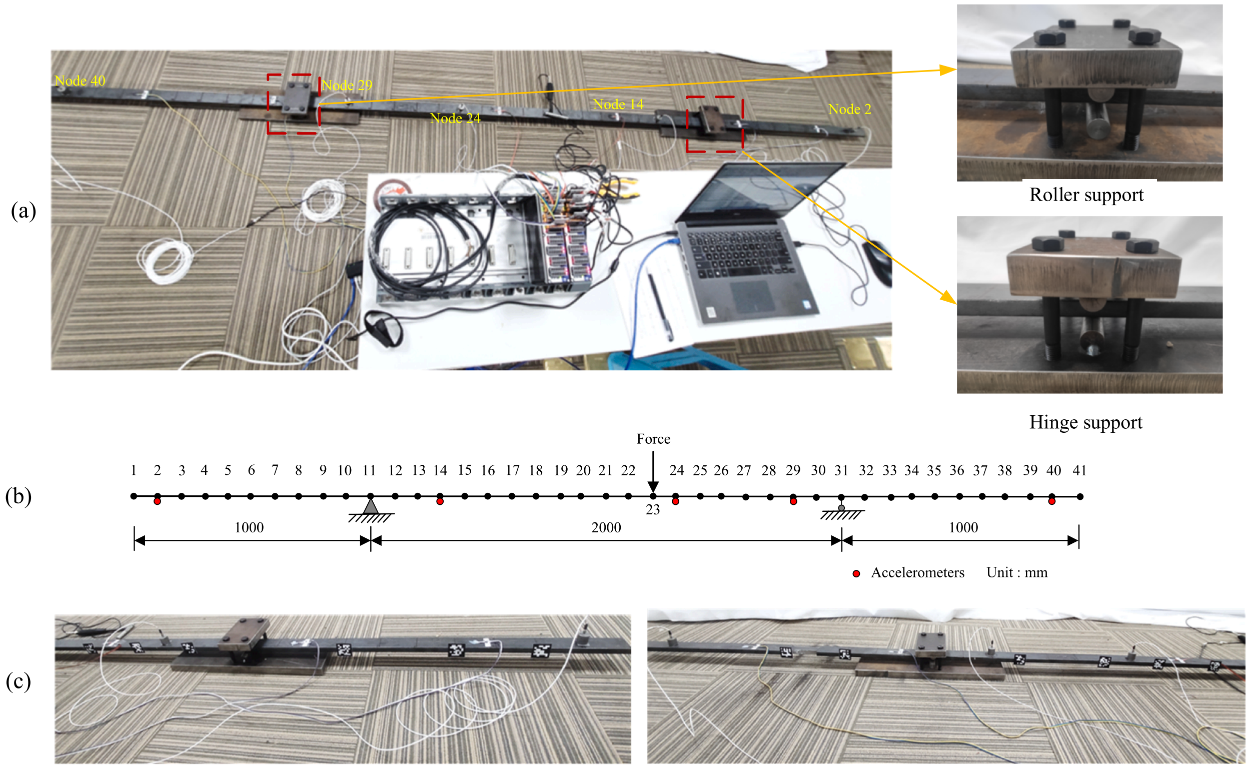

Fig. 15. Three-span beam structure: (a) experimental arrangement; (b) finite element model; (c) targets attached on the substructure.

generated by a force hammer with rubber tip is applied at node 23 of the beam. Five PCB-393B04 accelerometers are placed at nodes 2, 14, 24, 29 and 40 to measure structural dynamic responses, these signals are collected by MX 1601B data acquisition module and Quantum X data collection system. The masses of accelerometers are considered. In the laboratory test, sampling frequency is set as 300 Hz and sampling duration is 60 s.

Initial model updating is essential to make the finite element model represent the real three-span beam structure. The first three natural frequencies obtained from measured accelerations in the undamaged state are 5.669 Hz, 8.560 Hz, 17.345 Hz, calculated from initial finite element model are 5.629 Hz, 8.653 Hz, 17.452 Hz. The maximum relative error is 1.085 %, while the maximum discrepancy after model updating between the tested and numerical frequencies is just 0.162 %. By Table 4, these results imply the updated finite element model is accurate enough to be regarded as baseline for subsequent damage identification.

As shown in Fig. 16, the cross-section of three-span beam structure is artificially cut to introduce local damage. The symmetric 100 mm × 10 mm cross-section is reduced at element 6 and element 35, which results in 40 % equivalent stiffness reduction, i.e., $\alpha_6 = 0.4$, $\alpha_{35} = 0.4$.

5.2.2. Substructure *a*

As presented in Fig. 17, the 1st to 18th elements of the three-span beam structure is selected as the target substructure, named substructure *a*. Two interface forces are treated as unknown excitations. To obtain the displacement responses, six checkerboard targets with the size of 30 mm × 30 mm are attached on the surface of the beam at nodes 3, 5, 8, 13, 15, 17. A smartphone is used as a vision sensor to record the vibration histories in vertical direction with the sampling rate of 60 fps and a resolution of 3840 × 2160 pixel. Displacement time histories can be extracted by processing the video images frame by frame with the subpixel template matching algorithm. Then, they are divided into two sets. Measurement set 1 includes displacement response from nodes 3, 8, 13, 15, and measurement set 2 contains displacement responses from nodes 5 and 17. Obviously, the number of displacement responses in measurement set 1 is larger than the number of interface forces.

The measured displacement of node 3 in measurement set 1 is presented in Fig. 18. The displacement response at node 5 and node 17 in measurement set 2 are reconstructed to establish the objective function based on the discrepancy between the reconstructed and measured values, iteratively optimized with the proposed SQEA. The parameters are set the same values in Section 5.1.2. Damage identification results of substructure *a* are shown in Fig. 19. The damage extent at element 6 is 40.61 %, which is very close to the actual value 40 %. Some false identifications can be observed at elements 7, 10 and 14 but less than 2.1 %, possibly caused by measurement noise and model error. These results indicate that the proposed method could accurately detect, localize, and quantify substructural local damage.

Based on the identified parameters for substructure *a*, the reconstructed displacement responses at nodes 5 and 17 with are presented in Fig. 20. *RPE* and *PCC* are 4.89 % and 0.9988 for displacement at node 5, 6.20 % and 0.9981 for displacement at node 17. The reliable results prove the feasibility of non-contact vision-based displacement response reconstruction for substructure.

5.2.3. Substructure *b*

As shown in Fig. 21, the 19th to 40th elements of the three-span beam structure are chosen as the target substructure, termed as substructure *b*. There are one internal hammer force and two interface forces applied to the substructure *b*, treated as unknown excitations. Six targets are attached on the surface of the beam at nodes 21, 23, 25, 28, 34, 36. The vibration histories are recorded by a smartphone with the sampling rate of 60 fps and a resolution of 3840 × 2160 pixel. Displacement time histories in vertical direction are divided into two sets. Measurement set 1 includes displacement response from nodes 21, 23, 28, 34, and measurement set 2 contains displacement responses from nodes 25 and 36.

To test the optimization performance of the proposed SQEA, three current intelligent algorithms, i.e., improved Jaya algorithm (I-Jaya) [51], hybrid Jaya and differential evolution algorithm (HJDEA) [52], Q-learning evolutionary algorithm (QLEA) [43] are introduced to conduct damage identification for comparison purpose. These three algorithms are related to the proposed SQEA, so the improved performance of SQEA could be better verified. As regards the common parameters setting, population size is $NP = 100$ and the maximum number of iterations is $Max\_Iter = 200$. For the SQEA, maximum and minimum proportion parameters are $D_{e,\max} = 0.15$ and $D_{e,\min} = 0.4$. Discount factor is $\gamma = 0.8$. Fig. 22 presents the convergence process of objective function for I-Jaya, HJDEA, QLEA, SQEA, and their objective function values are 2.279, 0.266, 0.167, 0.0566. It is obvious that the SQEA can achieve more faster convergence speed than other three algorithm owing to integrating sparse population initialization, more diverse local search strategies.

The results calculated by these four algorithms are shown in Fig. 23. The location of damage element 35 is successfully detected and the identified damage extents are 29.26 %, 35.44 %, 36.80 %, and 39.01 % corresponding to I-Jaya, HJDEA, QLEA, and SQEA, respectively. In addition, by maximum and mean errors, as listed in Table 5, the proposed SQEA can yield more favorable performance than I-Jaya, HJDEA and QLEA, with less than 2.4 % maximum error and 0.6 % mean error. Some false identifications are clearly noticed at elements 19, 27, 34, 36 for I-Jaya, at elements 24, 32, 34 for HJDEA, at elements 29 and 39 for QLEA. Taking computational efficiency and identification accuracy into consideration, SQEA provides the most satisfactory performance.

6. Conclusions

In this paper, to deal with the limited FOV of consumer-grade camera in monitoring of large-scale and complex structures, a novel substructural damage identification method is developed based on the reinforcement learning guided evolutionary algorithm and vision-based response reconstruction technique. In the proposed method, multi-point displacement measurements of the target

Table 4
The measured and updated natural frequencies of three-span beam structure.

Mode	Before updating		After updating		Tested values from accelerations (Hz)
	Analytical (Hz)	Relative error (%)	Analytical (Hz)	Relative error (%)	
1	5.629	0.705	5.660	0.162	5.669
2	8.653	1.085	8.558	0.025	8.560
3	17.452	0.614	17.343	0.011	17.345

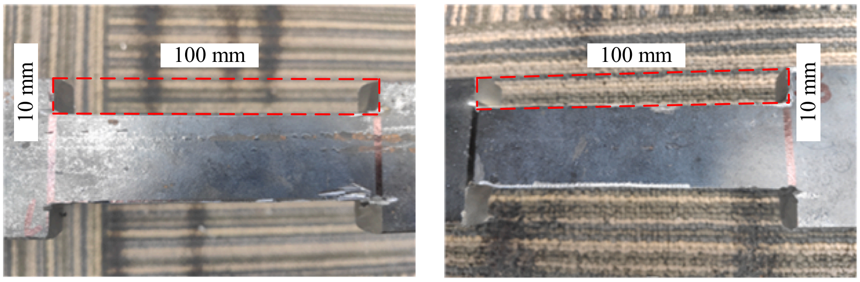

(a) 40% damage at the 6th element (b) 40% damage at the 35th element

Fig. 16. Introduced damage of the target substructure.

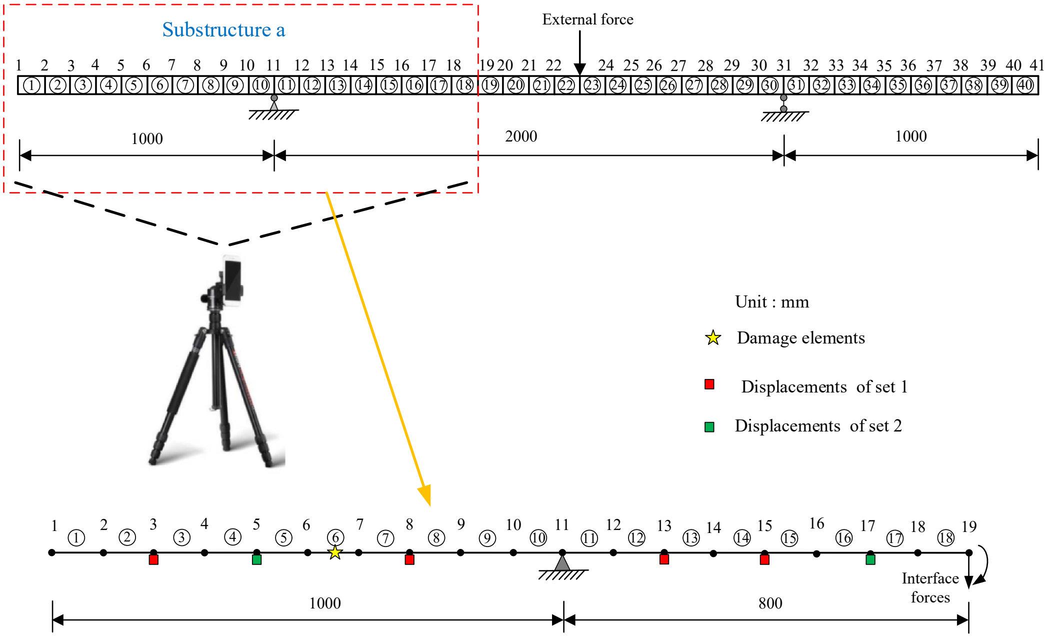

Fig. 17. The finite element model of the target substructure a.

substructure are obtained from the recorded video images and divided into two sets. The extracted displacement responses of set 2 are reconstructed with transmissibility matrix and measurement set 1 in time domain. The objective function is defined as the discrepancy between the measured and reconstructed displacement responses, optimized by a new sparse Q-learning guided optimization framework. Experimental studies on an eight-floor steel frame structure and a three-span beam structure are conducted to demonstrate the effectiveness of the proposed method. Some reliable conclusions can be drawn as follows:

(1) Substructural dynamic displacements can be accurately reconstructed using the non-contact vision-based displacement measurement and response reconstruction technique. The small values of *RPC* and *PCC* between the reconstructed and measured displacement responses validate the accuracy of the proposed method in displacement measurements and reconstruction for the large-scale and complex civil structure at some critical locations where no sensors installed.

(2) The locations and extents of local damage could be accurately identified with the proposed output-only substructural condition

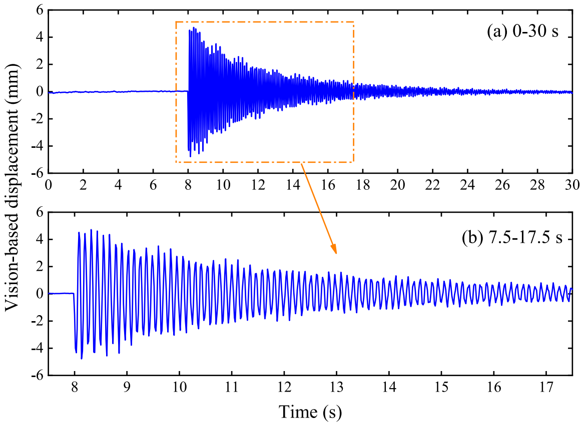

Fig. 18. The measured displacement of node 3 from video: (a) 0–30 s; (b) 7.5–17.5 s.

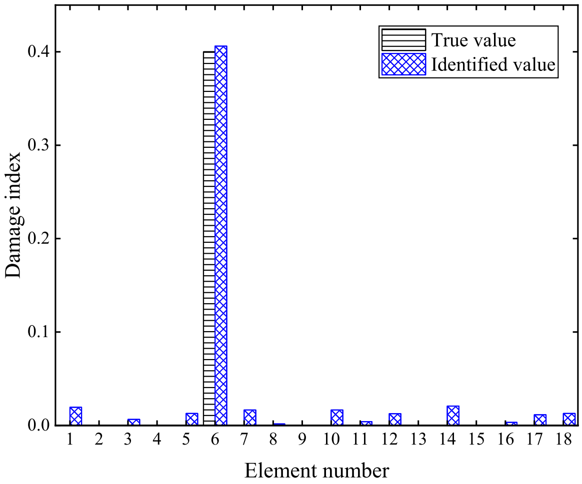

Fig. 19. Identification process of damage extent for substructure *a*.

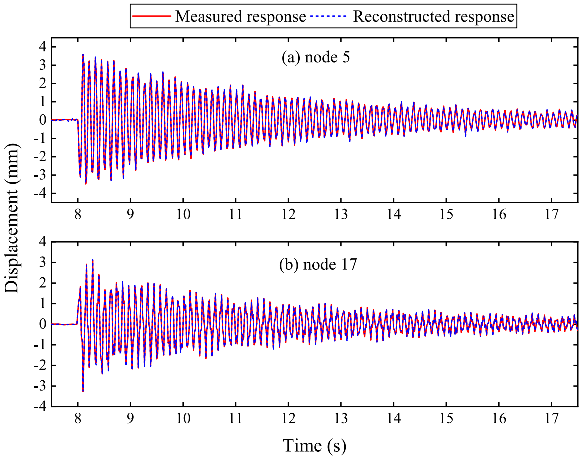

Fig. 20. Comparison of measured and reconstructed responses for substructure *a*: (a) node 5; (b) node 17.

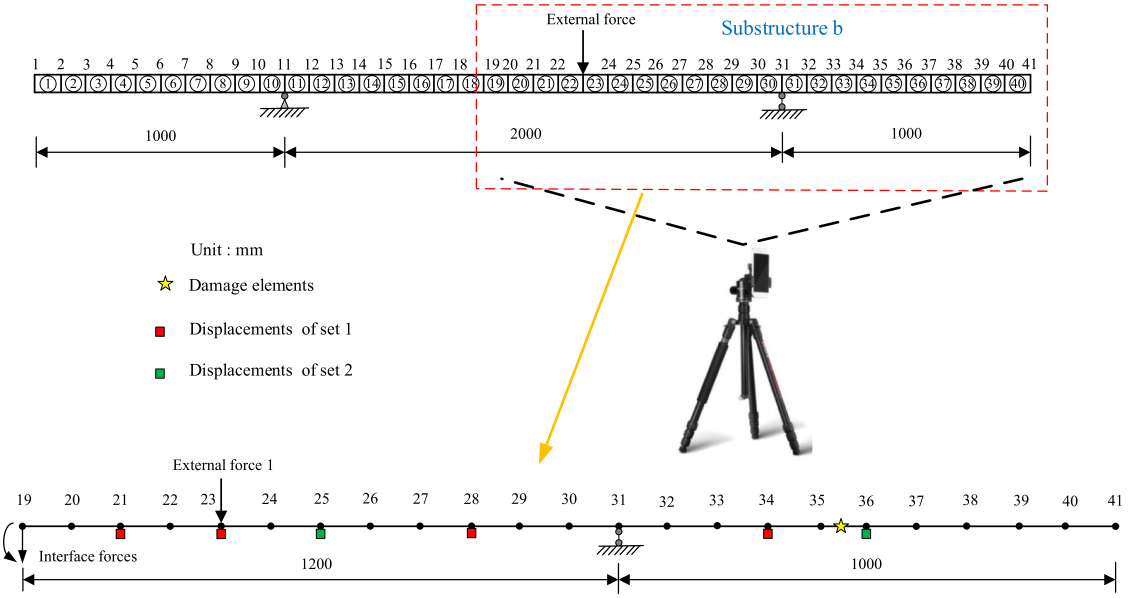

Fig. 21. The finite element model of the target substructure *b*.

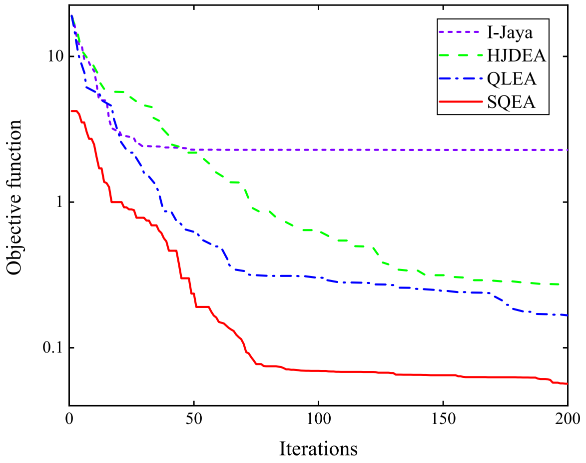

Fig. 22. The comparison of objective function for I-Jaya, HJDEA, QLEA, SQEA.

assessment method. The time histories of internal and interface forces are not required. The application of non-contact vision-based displacement measurement is successfully extended to substructural damage identification, significantly improving the identification accuracy and computational efficiency.

(3) The proposed SQEA could achieve faster convergence speed and more satisfactory identification results, compared with other current developed evolutionary algorithms, i.e., J-Jaya, HJDEA, QLEA, since sparse initial population is generated in search domain and the most appropriate search strategy is adaptively selected from the strategy pool under the guidance of Q-learning algorithm at each iteration.

The proposed method requires known locations of external excitations, which is challenging especially for structures under ambient excitations or traffic loads, limiting its practical applications to some extent. In order to quantify the severity of damage, an accurate FE model is needed. Additionally, the number of measurements within the first set surpasses or equals the unknown equivalent loads, which is essential for guaranteeing the success of pseudo-inverse, but difficult to achieve in certain conditions. Considering the success of the proposed method in dealing with the inverse problem of substructural damage identification, it can be extended to more practical civil structures, such as long-span bridges, tall buildings. Besides, data fusion including non-contact vision-based displacement measurement, accelerations and strains from contact sensors could be further investigated in the future.

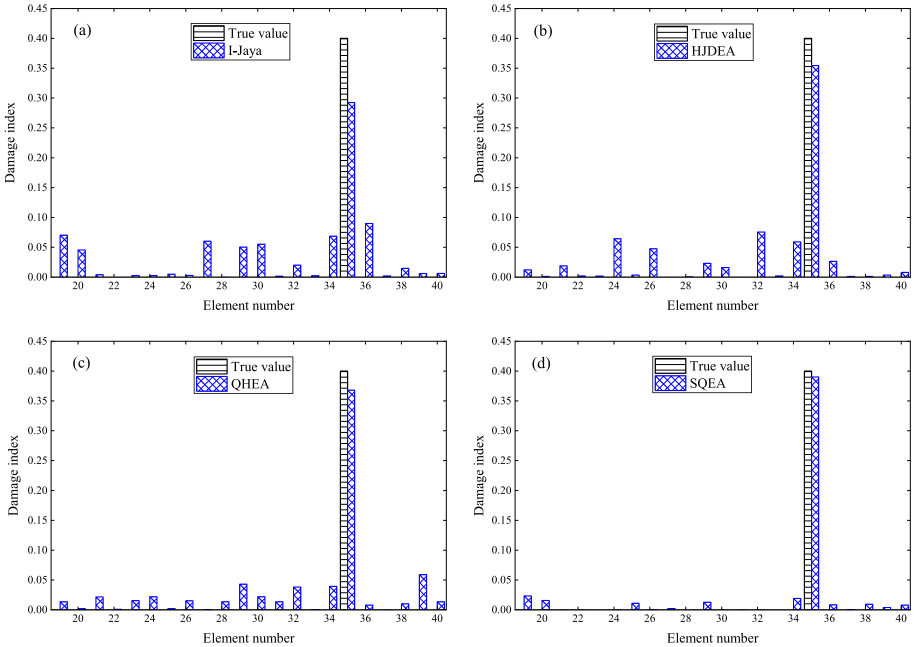

Fig. 23. Identified results of the target substructure *b* with: (a) I-Jaya; (b) HJDEA; (c) QLEA; (d) SQEA.

Table 5
The identified errors with I-Jaya, HJDEA, QLEA, SQEA (%).

Error	I-Jaya	HJDEA	QLEA	SQEA
Max error	10.74	7.54	5.89	2.32
Mean error	2.80	1.87	1.75	0.56
identified damage extent	29.26	35.44	36.80	39.01
Relative error	26.85	11.40	7.99	2.47

CRediT authorship contribution statement

Guangcai Zhang: Writing – original draft, Software, Methodology, Investigation, Conceptualization. **Jiale Hou:** Visualization, Validation, Methodology, Investigation. **Chunfeng Wan:** Writing – review & editing, Supervision, Conceptualization. **Jun Li:** Supervision. **Liyu Xie:** Writing – review & editing. **Songtao Xue:** Writing – review & editing, Funding acquisition.

Declaration of competing interest

The authors declare that they have no known competing financial interests or personal relationships that could have appeared to influence the work reported in this paper.

Data availability

Data will be made available on request.

Acknowledgments

This research is supported by: the National Key R&D Program of China (2021YFE0112200), Nanjing Major Project of Science and Technology, Research Fund for Advanced Ocean Institute of Southeast University (GP202409), and the Postgraduate Research&-Practice Innovation Program of Jiangsu Province (KYCX23_0273). The first author acknowledges China Scholarship Council (CSC 202306090271) to support visiting study in Curtin University.

References

[1] O. Avci, O. Abdeljaber, S. Kiranyaz, M. Hussein, M. Gabbouj, D.J. Inman, A review of vibration-based damage detection in civil structures: From traditional methods to Machine Learning and Deep Learning applications, Mech. Syst. Sig. Process. 147 (2021) 107077.

[2] A. Zar, Z. Hussain, M. Akbar, B.A. Tayeh, Z. Lin, A vibration-based approach for detecting arch dam damage using RBF neural networks and Jaya algorithms, Smart Struct. Syst. 32 (5) (2023) 319–338.
[3] Z. Chen, Q. Liu, Z. Ding, F. Liu, Automated structural resilience evaluation based on a multi-scale Transformer network using field monitoring data, Mech. Syst. Sig. Process. 222 (2025) 111813.
[4] G. Zhang, J. Hou, C. Wan, L. Xie, S. Xue, Structural system identification and damage detection using adaptive hybrid Jaya and differential evolution algorithm with mutation pool strategy, Structures. 46 (2022) 1313–1326.
[5] N. Bicanic, H.P. Chen, Damage identification in framed structures using natural frequencies, Int. J. Numer. Meth. Eng. 40 (23) (1997) 4451–4468.
[6] C.-X. Qu, T.-H. Yi, X.-J. Yao, H.-N. Li, Complex frequency identification using real modal shapes for a structure with proportional damping, Comput.-Aided Civ. Infrastruct. Eng. 36 (10) (2021) 1322–1336.
[7] K.D. Nguyen, T.H.T. Chan, D.P. Thambiratnam, A. Nguyen, Damage identification in a complex truss structure using modal characteristics correlation method and sensitivity-weighted search space, Struct. Health Monit. 18 (1) (2019) 49–65.
[8] L.T. Stutz, R.A. Tenenbaum, R.A.P. Correa, The Differential Evolution method applied to continuum damage identification via flexibility matrix, J. Sound Vib. 345 (2015) 86–102.
[9] M.J. Perry, C.G. Koh, Output-only structural identification in time domain: numerical and experimental studies, Earthquake Eng. Struct. Dyn. 37 (4) (2008) 517–533.
[10] Z. Ding, Y. Yu, D. Tan, K.V. Yuen, Adaptive vision feature extractions and reinforced learning-assisted evolution for structural condition assessment, Struct. Multidisc. Optim. 66 (9) (2023) 209.
[11] C.G. Koh, Y.-F. Chen, C.Y. Liaw, A hybrid computational strategy for identification of structural parameters, Comput. Struct. 81 (2) (2003) 107–117.
[12] C.-D. Zhang, Y.-L. Xu, Multi-level damage identification with response reconstruction, Mech. Syst. Sig. Process. 95 (2017) 42–57.
[13] Y. Li, L. Sun, Substructure-level damage identification based on the spectrum-probability space of the transmissibility function, J. Sound Vib. 571 (2024) 118117.
[14] C. Pan, Y. Qiu, X. Jiang, S. Peng, Simultaneous identification of impact force and structural local damage under pre-segmentation of structural elements, Structures. 57 (2023) 105186.
[15] M.-S. Huang, X. Cheng, Y.-Z. Lei, Structural damage identification based on substructure method and improved whale optimization algorithm, J. Civ. Struct. Heal. Monit. 11 (2021) 351–380.
[16] Y. Yang, Q. Jiang, A novel phase-based video motion magnification method for non-contact measurement of micro-amplitude vibration, Mech. Syst. Sig. Process. 215 (2024) 111429.
[17] K. Luo, X. Kong, J. Li, J. Hu, L. Deng, Motion magnification for video-based vibration measurement of civil structures: A review, Mech. Syst. Sig. Process. 220 (2024) 111681.
[18] M. Ghyabi, L.C. Timber, G. Jahangiri, D. Lattanzi, H.W. Shenton III, M.J. Chajes, M.H. Head, Vision-based measurements to quantify bridge deformations, J. Bridge Eng. 28 (1) (2023) 05022010.
[19] K. Luo, X. Kong, L. Deng, W. Ji, L. Meng, Target-free measurement of cable forces based on computer vision and equivalent frequency difference, Eng. Struct. 314 (2024) 118390.
[20] Y. Xu, J.M.W. Brownjohn, Review of machine-vision based methodologies for displacement measurement in civil structures, J. Civ. Struct. Heal. Monit. 8 (2018) 91–110.
[21] R. Kromanis, P. Kripakaran, A multiple camera position approach for accurate displacement measurement using computer vision, J. Civ. Struct. Heal. Monit. 11 (3) (2021) 661–678.
[22] E. Ozer, R. Kromanis, Smartphone Prospects in Bridge Structural Health Monitoring, a Literature Review, Sensors. 24 (11) (2024) 3287.
[23] L. Ge, K.Y. Koo, M. Wang, J. Brownjohn, D. Dan, Bridge damage detection using precise vision-based displacement influence lines and weigh-in-motion devices: Experimental validation, Eng Struct. 288 (2023) 116185.
[24] Z. Yi, M. Cao, Y. Kito, G. Sato, X. Zhang, L. Xie, S. Xue, Real-time displacement monitoring using camera video records with camera motion correction, Measurement. 114406 (2024).
[25] C.-Z. Dong, F.N. Catbas, A review of computer vision–based structural health monitoring at local and global levels, Struct. Health Monit. 20 (2) (2021) 692–743.
[26] D. Feng, M.Q. Feng, Identification of structural stiffness and excitation forces in time domain using noncontact vision-based displacement measurement, J. Sound Vib. 406 (2017) 15–28.
[27] D. Tan, J. Li, H. Hao, Z. Nie, Target-free vision-based approach for modal identification of a simply-supported bridge, Eng. Struct. 279 (2023) 115586.
[28] Y.J. Cha, J.G. Chen, O. Büyüköztürk, Output-only computer vision based damage detection using phase-based optical flow and unscented Kalman filters, Eng. Struct. 132 (2017) 300–313.
[29] S. Zhang, P. Ni, J. Wen, Q. Han, X. Du, J. Fu, Intelligent identification of moving forces based on visual perception, Mech. Syst. Sig. Process. 214 (2024) 111372.
[30] X. Gao, X. Ji, Y. Zhang, Y. Zhuang, E. Cai, Structural displacement estimation by a hybrid computer vision approach, Mech. Syst. Sig. Process. 204 (2023) 110754.
[31] E. Cai, Y. Zhang, X. Lu, X. Ji, Y. Li, J. Li, X. Song, H. Zhang, Y. Liu, Estimating small structural motions based on sparsity enforcement, Comput.-Aided Civ. Infrastruct. Eng. 38 (9) (2023) 1199–1216.
[32] E. Cai, Y. Zhang, X. Ji, X. Lu, L. Xie, Y. Zhuang, T. Zhao, G. Lin, Estimating small structural motions from multi-view video measurement, Eng. Struct. 275 (2023) 115259.
[33] K. Feng, A. González, M. Casero, A kNN algorithm for locating and quantifying stiffness loss in a bridge from the forced vibration due to a truck crossing at low speed, Mech. Syst. Sig. Process. 154 (2021) 107599.
[34] Q. Hu, N. Zhou, H. Chen, S. Weng, Bayesian damage identification of an unsymmetrical frame structure with an improved PSO algorithm, Structures. 57 (2023) 105119.
[35] N.B. Guedria, An accelerated differential evolution algorithm with new operators for multi-damage detection in plate-like structures, Appl. Math. Model. 80 (2020) 366–383.
[36] Z. Ding, K. Fu, W. Deng, J. Li, Z. Lu, A modified Artificial Bee Colony algorithm for structural damage identification under varying temperature based on a novel objective function, Appl. Math. Model. 88 (2020) 122–141.
[37] G. Zhang, C. Wan, L. Xie, S. Xue, Structural damage identification with output-only measurements using modified Jaya algorithm and Tikhonov regularization method, Smart Struct. Syst. 31 (3) (2023) 229–245.
[38] M. Huang, X. Cheng, Z. Zhu, J. Luo, J. Gu, A novel two-stage structural damage identification method based on superposition of modal flexibility curvature and whale optimization algorithm, Int. J. Struct. Stab. Dyn. 21 (12) (2021) 2150169.
[39] G. Zhang, J. Hou, K. Feng, C. Wan, L. Xie, S. Xue, M. Noori, Z. Ding, Structural damage identification with output-only strain measurements and swarm intelligence algorithms: a comparative study, Meas. Sci. Technol. 35 (5) (2024) 056125.
[40] H. Zhou, G. Zhang, X. Wang, P. Ni, J. Zhang, Structural identification using improved butterfly optimization algorithm with adaptive sampling test and search space reduction method, Structures. 33 (2021) 2121–2139.
[41] Y. Wu, F. Kang, Y. Zhang, X. Li, H. Li, Structural identification of concrete dams with ambient vibration based on surrogate-assisted multi-objective salp swarm algorithm, Structures. 60 (2024) 105956.
[42] Y. Zhang, K. Zhou, J. Tang, Harnessing Collaborative Learning Automata to Guide Multi-objective Optimization based Inverse Analysis for Structural Damage Identification, Appl. Soft Comput. 160 (2024) 111697.
[43] Z. Ding, L. Li, X. Wang, T. Yu, Y. Xia, Vibration-based FRP debonding detection using a Q-learning evolutionary algorithm, Eng. Struct. 275 (2023) 115254.
[44] D. Feng, M.Q. Feng, Vision-based multipoint displacement measurement for structural health monitoring, Struct. Control Health Monit. 23 (5) (2016) 876–890.
[45] M. Debella-Gilo, A. Kääb, Sub-pixel precision image matching for measuring surface displacements on mass movements using normalized cross-correlation, Remote Sens. Environ. 115 (1) (2011) 130–142.

[46] D. Feng, M.Q. Feng, E. Ozer, Y. Fukuda, A vision-based sensor for noncontact structural displacement measurement, Sensors. 15 (7) (2015) 16557–16575.

[47] G. Zhang, J. Kang, C. Wan, L. Xie, S. Xue, Output-only structural damage identification based on Q-learning hybrid evolutionary algorithm and response reconstruction technique, Measurement. 224 (2024) 113951.

[48] T.N. Huynh, D.T.T. Do, J. Lee, Q-Learning-based parameter control in differential evolution for structural optimization, Appl. Soft Comput. 107 (2021) 107464.

[49] D. Calvetti, S. Morigi, L. Reichel, F. Sgallari, Tikhonov regularization and the L-curve for large discrete ill-posed problems, J. Comput. Appl. Math. 123 (1–2) (2000) 423–446.

[50] H. Sun, O. Büyüköztürk, Identification of traffic-induced nodal excitations of truss bridges through heterogeneous data fusion, Smart Mater. Struct. 24 (7) (2015) 075032.

[51] Z. Ding, J. Li, H. Hao, Structural damage identification using improved Jaya algorithm based on sparse regularization and Bayesian inference, Mech. Syst. Sig. Process. 132 (2019) 211–231.

[52] G. Zhang, C. Wan, X. Xiong, L. Xie, M. Noori, S. Xue, Output-only structural damage identification using hybrid Jaya and differential evolution algorithm with reference-free correlation functions, Measurement. 199 (2022) 111591.